UNIVERSITY OF CALIFORNIA,
IRVINE

Automated Extraction of Glacial Features using Deep Learning

DISSERTATION

submitted in partial satisfaction of the requirements
for the degree of

DOCTOR OF PHILOSOPHY

in Computer Science

by

Daniel Cheng

Dissertation Committee:
Associate Professor Wayne Hayes, Chair
Professor Charless Fowlkes
Professor Xiaohui Xie

2021

TABLE OF CONTENTS

LIST OF FIGURES

LIST OF TABLES

ACKNOWLEDGMENTS

I would like to extend my thanks and appreciation to my advisor Wayne Hayes, whose advice, guidance, and encouragement have been instrumental in shaping my current and future paths. His generous offers of time and effort during my undergraduate years, and his continued support through my graduate studies have no doubt shaped and enabled me to fulfill my potential, and continue my growth moving forward.

I give my appreciation and thanks to Eric Larour, for his guidance and mentorship from an undergraduate to a graduate student and beyond. His logistical, scientific, and personal backing of my endeavors have allowed me to become achieve great strides as a student and a scientist, for which I am immensely grateful.

Thank you Nicole Schlegel and Mathieu Morlighem, along with the members of the Ice Sheet and System Model Team at NASA-JPL/UC-Irvine, for their continued mentorship, support, and assistance over the years. I greatly appreciate the time and effort from them to make my experience in the team a welcoming one, with much opportunity for growth and development.

Thanks to Charless Fowlkes and Xiaohui Xie for providing the time and guidance needed to better develop the machine learning techniques utilized in my studies, as well as their feedback on this very thesis.

I am grateful for the support of my friends at UC Irvine, who have supported me academically and socially, and humoured many a discussion throughout our times together.

And to my parents, I am immensely grateful for providing the best environment one could ask for throughout my entire life. I very much appreciate them for allowing me to pursue these studies with a dedication matched only by their own to support for me.

VITA

Daniel Cheng

EDUCATION

Doctor of Philosophy in Computer Science **2021**
University of California, Irvine *Irvine, California*

Master of Science in Computational Sciences **2019**
University of California, Irvine *Irvine, California*

Bachelor of Science in Computer Science and Engineering **2017**
University of California, Irvine *Irvine, California*

RESEARCH EXPERIENCE

Undergraduate Student Researcher **2014–2016**
University of California, Irvine *Irvine, California*

Student Intern **2014–2021**
NASA Jet Propulsion Laboratory *Pasadena, California*

TEACHING EXPERIENCE

Teaching Assistant **2017–2021**
University of California Irvine *Irvine, California*

REFEREED JOURNAL PUBLICATIONS

Helheim Glacier's terminus position controls its seasonal and inter-annual ice flow variability — **November 2021**
Geophysical Research Letters, in submission

A century ofGreenland glacier terminus data for use in machine learning applications — **October 2021**
The Cryosphere Discussions, in review

Calving front machine (CALFIN): Glacial termini dataset and automated deep learning extraction method for Greenland, 1972-2019 — **April 2021**
The Cryosphere

A JavaScript API for the Ice Sheet System Model (ISSM) 4.11: towards an online interactive model for the cryosphere community — **December 2017**
Geosci. Model Dev.

REFEREED CONFERENCE PUBLICATIONS

CALFIN: A Calving Front Mask Dataset for Greenland, 1972-2019 — **December 2020**
American Geophysical Union Fall Meeting

Calving Front Machine (CALFIN): A Calving Front Mask Dataset for West Greenland, 1972-2018 — **April 2019**
European Geosciences Union General Assembly

Calving Front Machine (CALFIN): A calving front mask dataset for West Greenland, 1972-2018 — **December 2018**
American Geophysical Union Fall Meeting

VESL: The Virtual Earth Sheet Laboratory for Ice Sheet Modeling and Visualization — **December 2017**
American Geophysical Union Fall Meeting

Cryosphere Science Outreach using the NASA/JPL Virtual Earth System Laboratory — **December 2016**
American Geophysical Union Fall Meeting

Leveraging Cloud Technology to Provide a Responsive, Reliable and Scalable Backend for the Virtual Ice Sheet Laboratory Using the Ice Sheet System Model and Amazon's Elastic Compute Cloud — **December 2015**
American Geophysical Union Fall Meeting

ABSTRACT OF THE DISSERTATION

Automated Extraction of Glacial Features using Deep Learning

By

Daniel Cheng

Doctor of Philosophy in Computer Science

University of California, Irvine, 2021

Associate Professor Wayne Hayes, Chair

Sea level contributions from the Greenland Ice Sheet are influenced by the rapid changes in glacial terminus positions. Also known as *calving front* positions this information is captured in satellite imagery, but determining the position of the actual front usually involves laborious human labor, causing a major bottleneck in processing the thousands of existing images. From Landsat satellite imagery, we face the task of generating 22,678 calving fronts across 66 Greenlandic glaciers. Automated methods face challenges that include the handling of clouds, illumination differences, sea ice mélange, and Landsat-7 Scanline Corrector Errors. To address these needs, we develop the Calving Front Machine (CALFIN), an automated method for extracting calving fronts from satellite images of marine-terminating glaciers, using neural networks. CALFIN builds upon existing neural network architectures, and specializes in the segmentation of line-like features, while simultaneously handling large amounts of noise in the source data. Novel post-processing algorithms are used to perform the feature extraction and vectorization. The results are often indistinguishable from manually-curated fronts, deviating by on average 2.25 ± 0.03 pixels (86.76 ± 1.43 meters) from the measured front. This improves on the state of the art in terms of the spatio-temporal coverage and accuracy of its outputs, and is validated through a comprehensive intercomparison with existing studies. The current implementation offers a new opportunity to explore sub-seasonal and regional trends on the extent of Greenland's margins, and supplies new constraints for

simulations of the evolution of the mass balance of the Greenland Ice Sheet and its contributions to future sea level rise.

Chapter 1

Introduction

Derived from: Cheng, D., Hayes, W., Larour, E., Mohajerani, Y., Wood, M., Velicogna, I., & Rignot, E. (2021). Calving Front Machine (CALFIN): Glacial termini dataset and automated deep learning extraction method for Greenland, 1972–2019. The Cryosphere, 15(3), 1663–1675. https://doi.org/10.5194/tc-15-1663-2021

1.1 Background

Sea level contributions from the ice sheets are influenced by the ice-ocean interactions along their rapidly changing margins. The understanding of these processes, the changing margins, and their effects on ice sheets as a whole is therefore important [Nick et al., 2013]. In particular, contributions from the Greenland's glaciers are needed to assess the overall impact of the Greenland Ice Sheet (GrIS) on global mean sea level rise (GMSLR) over the next century [Andersen et al., 2015; Fürst et al., 2015; van den Broeke et al., 2016]. Already in the past 25 years, the sea level has risen approximately 3mm/yr [Group, 2018].

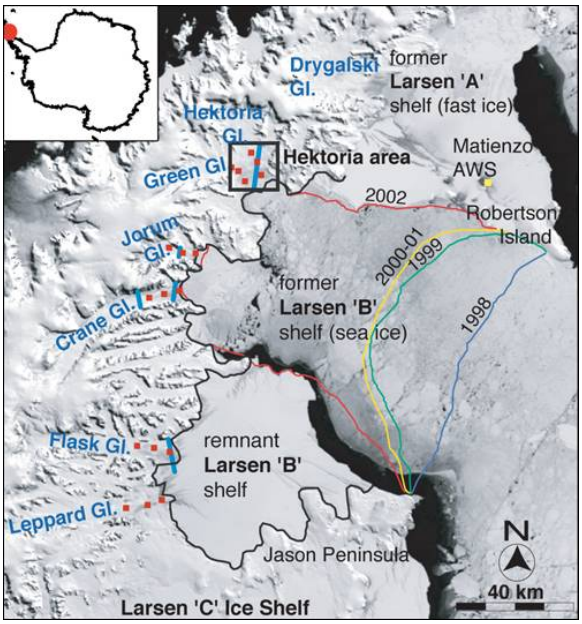

Figure 1.1: **Antarctica Ice Sheet, Larsen B Ice Shelf Collapse**. Larsen B experienced significant retreat even before its collapse in 2002. Studying its evolution in the years preceding and proceeding its collapse will be important for understanding the contributing processes. Figure derived from [Scambos et al., 2004].

Concerningly, GMSLR contributions from the melting of the GrIS has increased from less than 5% of the total change during 1993 to more than 25% during 2014 [Chen et al., 2017]. Critically, the physical processes responsible for the evolution of the ice sheets are not yet fully understood. In Antarctica, ice shelves such as Larsen B and C have been identified as to be susceptible to among the most vulnerable ice shelves accounting for future surface melt and runoff scenarios [Gilbert and Kittel, 2021]. And while recent studies have established that the collapse of Larsen B (see Figure 1.1) was the result of surface processes [Rebesco et al., 2014], the topic of which processes - and to what degree each contributes - is still not definitively known. A better understanding of the processes underlying the vulnerability of ice sheets and shelves can therefore benefit modeling efforts by informing the areas where they are being actively developed [Larour et al., 2021]. These processes include the interactions between rifts/fractures, ice mélange, grounding lines, melt pond induced hydrofracture, ocean/atmospheric temperatures, and in particular, calving fronts.

While there are publicly accessible time series records of rift/fracture [Marsh et al., 2021], melt pond [Stokes et al., 2019], and calving front Cheng et al. [2021]; Baumhoer et al. [2019] positions, there are no consolidated approaches that examine the inter-annual and seasonal variations in such time series records. Consequently, these variations and their effects on the stability of ice sheets are not well constrained.

It follows that if accurate representations of the physical features in ice sheets such as the GrIS can be obtained, climate modeling and analysis can be carried out on the parameterizations of such features with other ice sheet inputs, and their dominant contributions to glacial and ice shelf evolution - and therefore the GMSLR - can be constrained.

1.2 Relevance to existing work

Recent studies of physical ice shelf controls propose competing explanations for the dominant processes affecting ice shelf vulnerability [Lai et al., 2020; Larour et al., 2021]. In melt-pond induced hydrofracture, meltwater from radiative and atmospheric conditions collects in ponds distributed across surface of the ice shelf, and seeps into fractures or crevasses within the shelf. This results in stress applied by hydrostatic pressure to fracture tips, and can be exacerbated by repeated cycles of melting/refreezing, resulting in fracture propagation throughout the ice shelf. This process is proposed to be dominant across the AIS in [Lai et al., 2020]. In another process, thick ice mélange within rifts can transmit compressive/shear stresses, slowing rift propagation significantly. However, ocean and atmospheric temperatures can thin ice mélange within rifts and trigger a loss in mechanical integrity within the ice mélange, resulting in rift propagation and calving. These examples highlight the general need for more extensive analyses of ice shelf processes as they relate to ice sheet vulnerability [Khazendar et al., 2007], in order to better constrain their contributions to future changes in the GMSLR.

In the GrIS, a significant form of ice mass loss and GMSLR contributions is due to changes in marine terminating glaciers, and calving front evolution in particular. While satellite imagery allows for the extensive capturing of this evolving constraint, most calving front delineation is still done with time-consuming manual labor [Carr et al., 2017; Bunce et al., 2018; Catania et al., 2018]. This results in the under-utilization of available satellite imagery, and causes gaps in seasonal records that introduce uncertainty when modeling past and projected climate change [Catania et al., 2020]. Significant efforts have been made to improve this situation, which include the ESA-CCI dataset of 26 Greenlandic glaciers from 1990-2016, the PROMICE dataset of 47 glaciers from 1990-2018, and the MEaSUREs dataset of 200+ glaciers from 2000-2017 [ENVEO, 2017; Andersen et al., 2019; Joughin et al., 2015]. Yet the increasing availability of new datasets through missions like Landsat 8 and the release of old datasets through improved reprocessing call for new automated ways of detecting the glacial features such as calving fronts.

Climate modeling presents a strong need for automated glacial feature extraction methods, which requires these methods to be robust against cloud cover, ice mélange, shadows, and issues like Landsat 7 Scanline Corrector Errors. Traditional automated techniques such as the edge detection utilized by Seale et al. [2011] and Paravolidakis et al. [2016] have significant challenges with respect to these issues. Modern machine learning techniques and deep neural networks provide a robust, scalable, and accurate solution to these processing challenges. Existing work by Mohajerani et al. [2019] pioneers the usage of these techniques by applying the Ronneberger et al. [2015] UNet deep neural network for Jakobshavn, Helheim, Sverdrup, and Kangerlussuaq Glaciers. It achieves a mean distance error of 96.3 m, but is restricted by the preprocessing requirement of aligning the flow direction to be vertical, and inability to handle branching/non-linear calving fronts. Zhang et al. [2019] evaluates a modified UNet applied to TerraSAR-X data over Jakobshavn Glacier, and achieves a mean distance error of 104 m, but is limited in scope. Baumhoer et al. [2019] expands the application of the UNet to Sentinel 1 imagery of Antarctica, extracting full coastline delineations and achieving a

mean distance error of 108 m. Ultimately, these case studies provide the groundwork for the automatic, accurate, large scale, long time-series, high temporal resolution, and potentially multi-sensor extraction of glacial terminus positions.

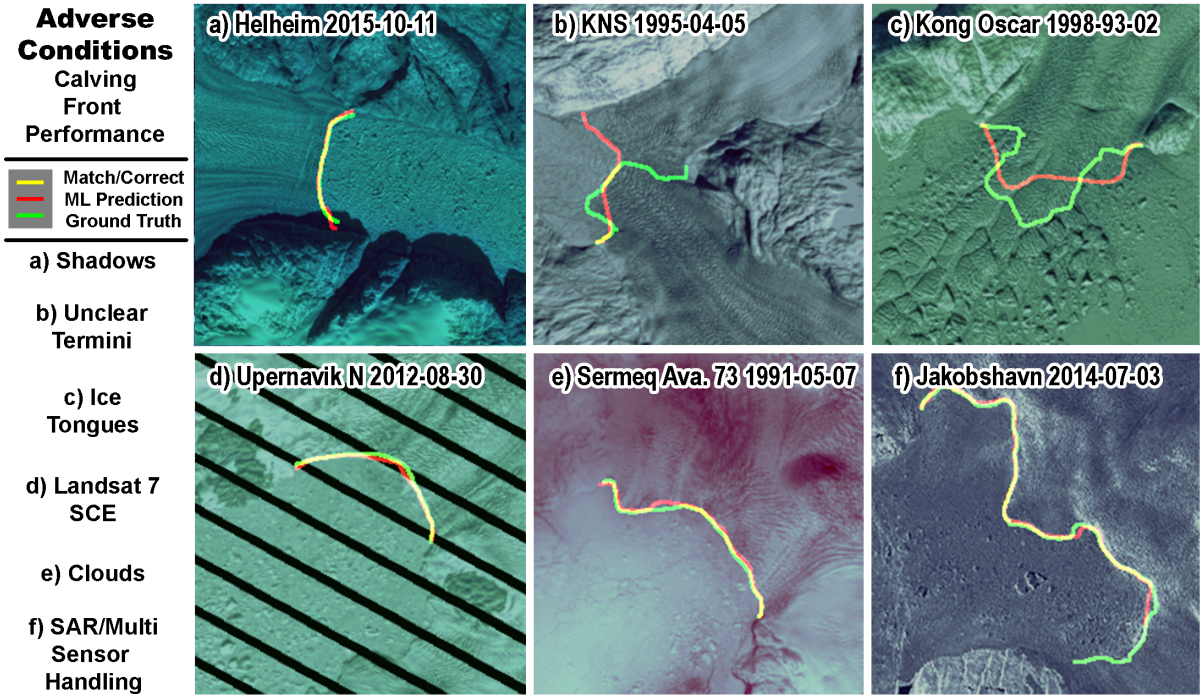

Figure 1.2: **Labeling Issues and Conditions**. An example of the various non-trivial issues and conditions associated with the available source data, which an automatic glacial feature extraction method must handle in order to accurately and effectively produce outputs.

1.3 Data Source and Scope

In order to study these changes, and produce the relevant calving front data products, a variety of existing satellite source data (as seen in Table 1.1) are evaluated and prepared for further processing.

Source Name	**Start Date**	**End Date**	**Spatial Res. (m)**	**Temporal Res. (days)**	**Sensor Type**
ASTER	01-2000	11-2020	15-19	16	Multispectral
Landsat 1	07-1972	01-1978	80	18	Multispectral
Landsat 2	01-1975	08-1983	80	18	Multispectral
Landsat 3	03-1978	09-1983	80	18	Multispectral
Landsat 4	07-1982	12-1993	30	16	Multispectral
Landsat 5	03-1984	01-2013	30	16	Multispectral
Landsat 7	04-1999	Ongoing	30	16	Multispectral
Landsat 8	02-2013	Ongoing	30	16	Multispectral
Sentinel 1	04-2014	Ongoing	20	6-12	SAR
Sentinel 2	06-2015	Ongoing	10	12	Multispectral
SPOT-1	02-1986	12-1990	20	26	Multispectral
ALOS-PALSAR	01-2006	04-2011	10-20	14	SAR
ENVISAT	03-2002	04-2012	30	35	SAR
ERS-1	07-1991	03-2000	30	3, 35, and 168	SAR
ERS-2	04-1995	09-2011	30	3, 35, and 168	SAR
JERS-1/ Fuyo-1	02-1992	10-1998	18	44	SAR
TerraSAR-X	01-2008	12-2020	40	11	SAR
RADARSAT 1	11-1995	03-2013	100	11	SAR

Table 1.1: **Publicly Available Satellite Imagery Sources**. Sensor type denotes whether or not Multispectral (visual/optical) or SAR (Synthetic Aperture Radar) instruments were used to generate imagery, where SAR imagery has the benefit of penetrating cloud cover and ignores shadows/illumination differences, but is only available at later start dates. Derived from Goliber et al. [2021].

The primary source data we selected is the Landsat series of optical images, which are used for their long time-series availability and reasonable spatial distribution/resolution. The area of interest for the dataset production is restricted to Greenland, in particular the calving fronts for 66 Greenlandic basins shown in Fig. 1.3, spanning the 1972 to 2019 time period shown in Fig. 1.4. The basins are selected for their high discharge volumes, wide spatial distribution, and diverse morphological features. The product used is the 60/30 meter resolution Near Infrared band. The 15 meter resolution panchromatic band was not used, due to computational and logistical limitations. A unique characteristic of this data source is the presence of Landsat 7 Scanline Corrector Errors from 2003-2013, which manifests as black stripes that interfere with automated calving front extraction methods.

For the training and validation of the methodology (covered in the following Chapter 2), we added TerraSAR-X and Sentinel 1A/B SAR images to enforce the applicability of the method across different sensors and domains. The area of interest for the training and validation of the methodology thus includes Antarctic SAR data in addition to the Greenlandic Landsat optical data (see Sect. 2.2 and Fig. S4). The TerraSAR-X product used is the StripMap 3 meter resolution HH polarization band. The Sentinel 1A/B product used is the Extra Wide Swath, Ground Range Multi-Look Detected, 40 meter resolution HH polarization band. The other data products and polarization bands are not used since the backscatter intensity provides sufficient information for the data processing methodology to succeed. A characteristic of SAR data is the presence of speckle noise, which is addressed by the methodology described in the following section.

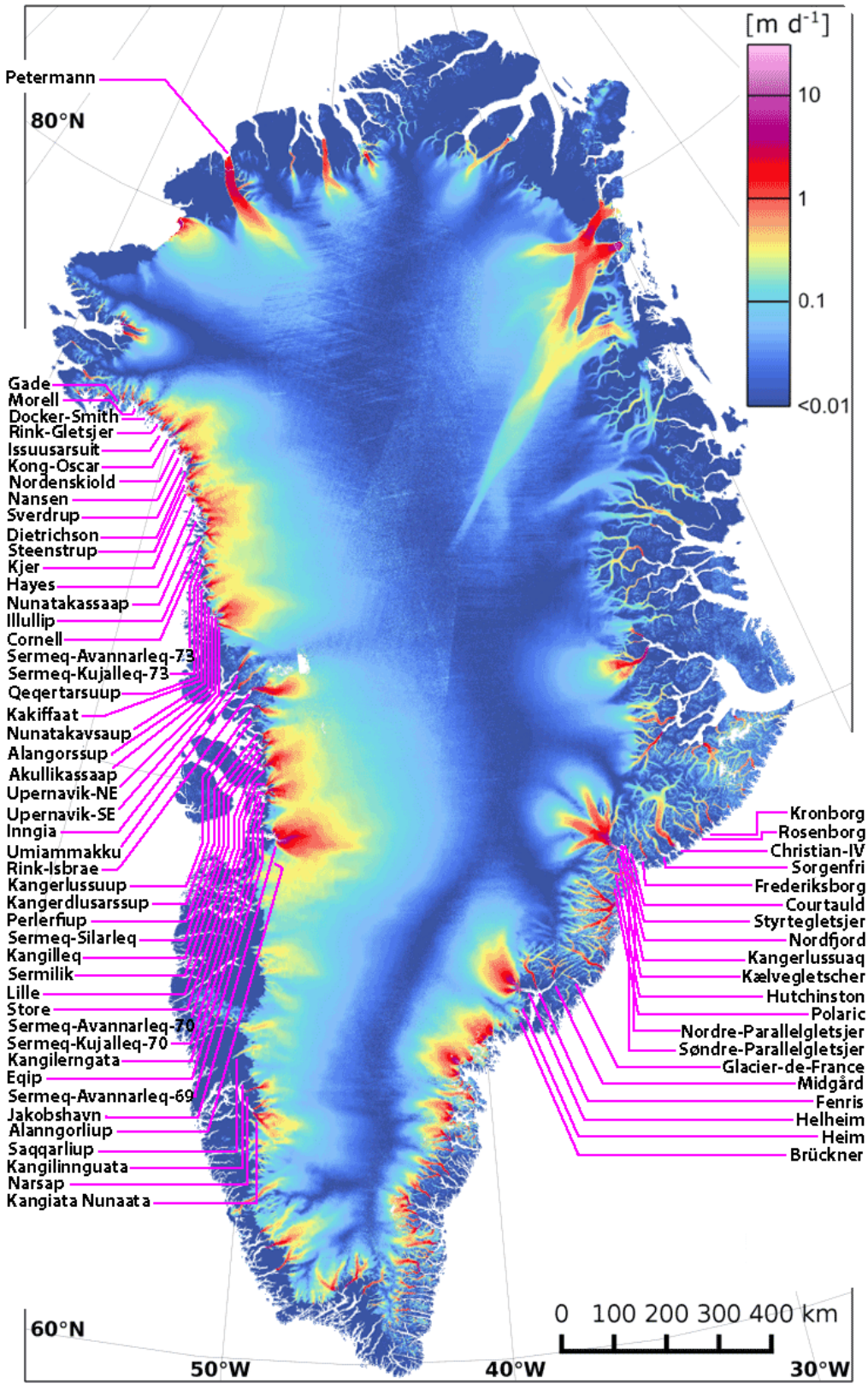

Figure 1.3: **Spatial Coverage Map**: Spatial distribution of 66 selected Greenlandic glaciers. The velocity map is taken from Nagler et al. [2015].

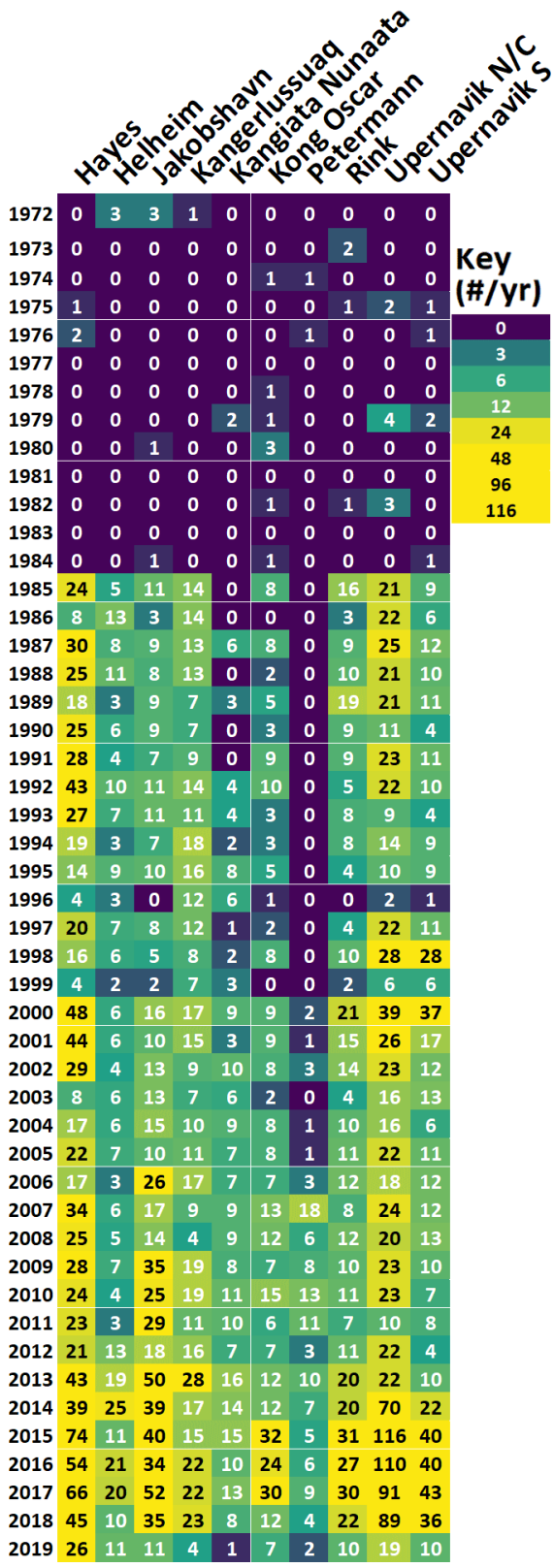

Figure 1.4: **Temporal Coverage Map**: Number of fronts per year from 1972-2019 for 10 high discharge volume basins. For the full temporal coverage map, see Appendix Fig. A1.

1.4 Outline of the Thesis

It is this groundwork on which the following chapters describe the CALFIN approach to address this problem. Each of the confounding non-trivial issues mentioned previously (and shown in Figure 1.2) is dealt with in order to effectively process the full breadth of available source data from satellite imagery. The processed outputs take the form Shapefiles that encode the spatial and temporal evolution of Greenland's glacial calving fronts. Each of these Shapefile outputs can encode the geographic coordinates that describe the glacial calving front positions, along with metadata statistics such as the time, quality, the latitudinal/longitudinal centers, source ID, and associated glacial IDs/names. These Shapefile outputs can then be used by glacial monitoring studies, cryospheric modeling programs such as the Ice-sheet and Sea Level Model [Larour et al., 2012], and contribute useful information in continuing efforts to address climate change.

Overall, the science goal of this work is to understand the interactions between the Greenland Ice Sheet (GrIS) and the ocean around it, and how it might affect the evolution of the ice and how much it will contribute to the Global Mean Sea Level Rise. In pursuit of this goal, the specific objective is to assess the feasibility of achieving robust automatic glacial calving front extraction for a selection of glaciers within the GrIS glaciers, and to provide the resulting dataset for use by the wider community. Additionally, this work contributes improvements to the neural network design for glacial feature extraction and post-processing methods.

The following Chapter 2 examines the CALFIN algorithm and method for processing the data. Chapter 3 validates the algorithm through error analysis. Chapter 4 shows the results - the calving front dataset and algorithm. Chapter 5 concludes with potential future work and research directions.

Chapter 2

Methododolgy

Our automated data processing methodology uses innovative techniques and state-of-the-art neural networks to process raw Landsat and Sentinel 1A/B data into useful calving front Shapefiles. The following section explores this methodology, as outlined by the flowchart below (Fig. 2.1).

2.1 Preprocessing

The first stage involves preprocessing the input data for use with the neural network, as illustrated in Fig. 2.2. The proceeding steps cover the details of handling Landsat data, but can be applied to Sentinel 1 data for validation purposes. To begin, raster images are selected from areas centered around one of 9 primary glacial basins. These basins include Kong Oscar, Hayes, Rink Isbrae, Upernavik, Jakobshavn, Kangiata Nunaata, Helheim, Kangerlussuaq, and Petermann. Next, all L1TP (precision and terrain corrected) rasters from Landsats 1-8 with low cloud coverage (<20%) are collected. A few L1GS/L1GT (non-corrected) products are also selected, which are manually georeferenced, and used to fill in Landsat 1-2 time

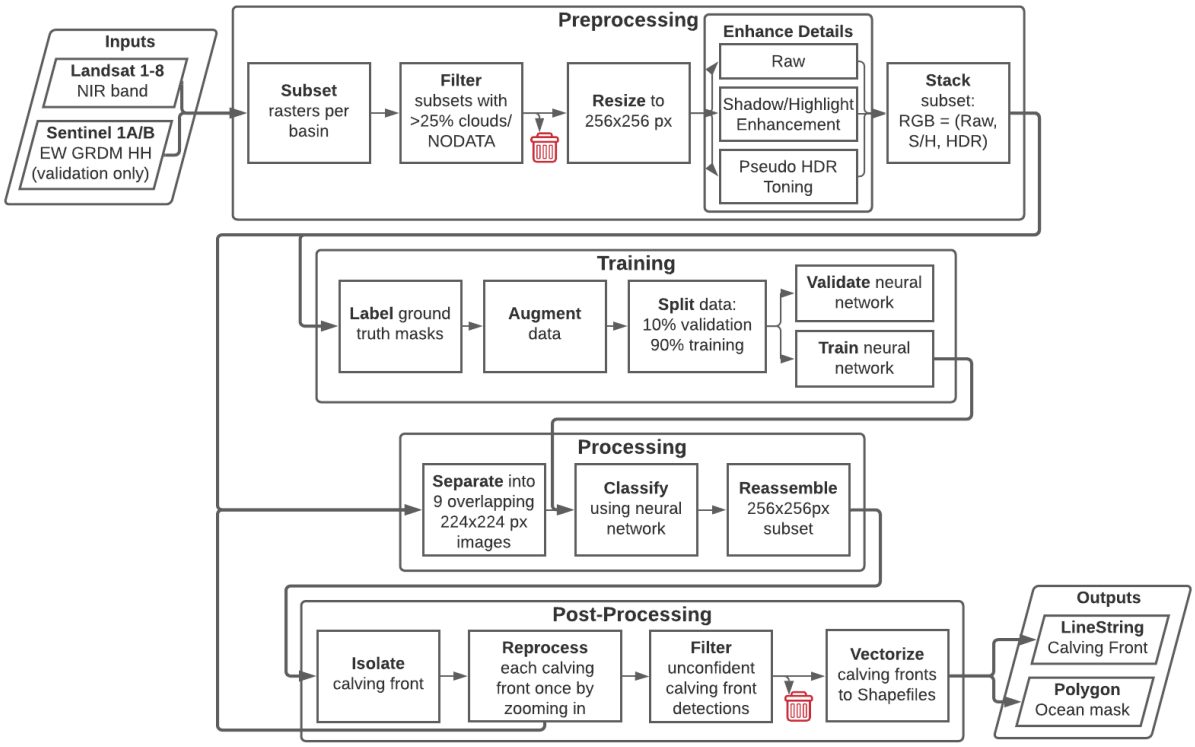

Figure 2.1: **Methodology Flowchart**: The CALFIN workflow, which processes single band raster imagery into calving front and ocean mask Shapefiles. Note that Sentinel 1A/B imagery is only used for validation, as it is not corrected and thus not qualified for geolocation/extraction.

series gaps (1972-1985). This results in a total of 4956 Landsat rasters. Next, predefined basin domain Shapefiles that enclose the terminus are used to clip the Landsat raster subsets. Additional filtering removes subsets that still contain $\geq$30% NODATA pixels or $\geq$20% cloud pixels detected in the Landsat QA band, as subsets that exceed these thresholds are not likely to contain detectable fronts. At this stage, 20188 GeoTIFF subsets are accumulated. Each subset is then resized to 256x256 px, and lastly enhanced using Pseudo-HDR Toning (HDR) and Shadows/Highlights (S/H) through Adobe Photoshop. The raw, HDR, and S/H enhanced subsets are then stacked into a single RGB image. At this point, the images are ready for processing into calving front masks.

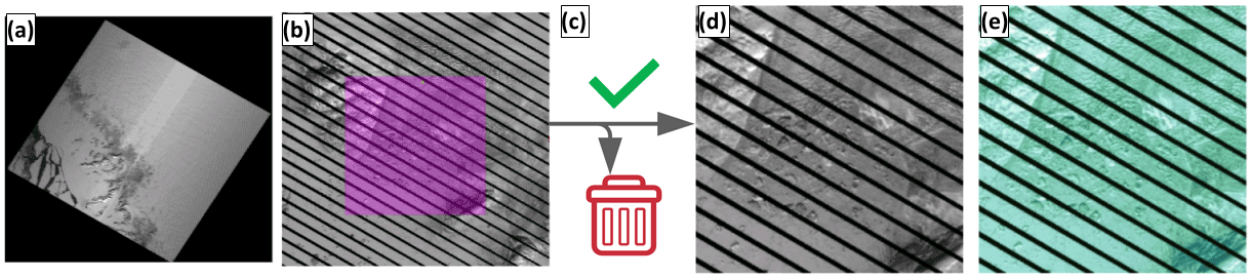

Figure 2.2: **Preprocessing Pipeline**: (a) First, input the raw Landsat GeoTIFF rasters with <20% clouds. (b) Next, subset using QGIS/GDAL and the domain Shapefile to clip each raster. (c) Then, filter the clouded/NODATA subsets. (d) Now, resize the subsets to 256x256 px. (e) Finally, enhance contrast and stack with the raw subset.

2.2 Neural Network Processing

Images are processed using the Calving Front Machine Neural Network (CALFIN-NN), as illustrated in Fig. 2.3. Neural networks like CALFIN-NN work by learning patterns in training data, and finding them in new data. CALFIN-NN is trained using manually delineated calving front masks. Once trained, CALFIN-NN outputs a probability mask that shows each pixel's likelihood of lying on the coastline/calving front. CALFIN-NN also generates a ice/ocean probability mask as a secondary output. Following this, the calving front is extracted during post-processing, discussed in Sect. 2.3.

Neural networks are the foundation of several automated delineation methods, including Mohajerani et al. [2019], Zhang et al. [2019], and Baumhoer et al. [2019]. This method builds upon this work, and uses a modification of the DeepLabV3+ Xception neural network from Chen et al. [2018], as shown in Fig. 2.3. The first half, the encoder, uses the Xception-65 network to extract image features [Chollet, 2017]. It does this by assembling basic features, like edges and corners, into more abstract features, such as glacier/land textures. The second half of the network, the decoder, takes the output of the encoder and up-samples the features to predict the final probability mask outputs.

Several architectural modifications are made to the original DeepLabV3+ Xception model

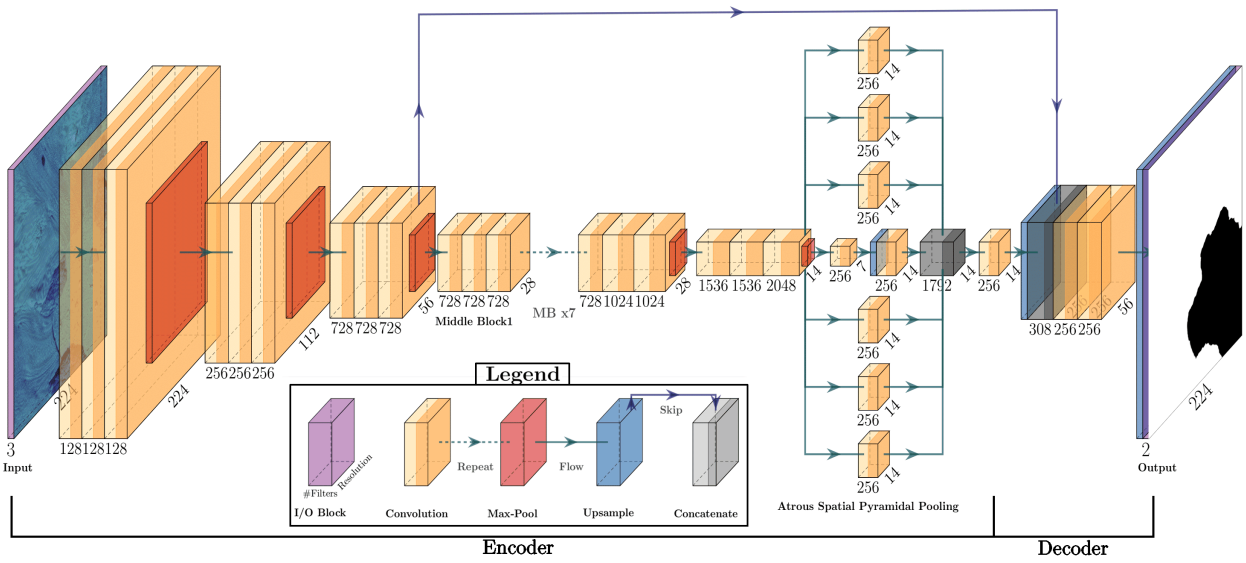

Figure 2.3: **The CALFIN-NN Processing Architecture**: Each orange "Xception" block consists of convolution kernels that detect features in the previous block. Blocks are reduced in size periodically to pool increasingly complex and numerous feature maps. "U" shaped connections help refine the probability masks during up-sampling. Note that the 7 repeated "Xception" blocks in the middle section are omitted for brevity.

to enhance its performance. To accurately recognize line-like features such as calving fronts, additional Atrous Spatial Pyramidal Pooling (ASPP) blocks are added in between the encoder and decoder, with the dilation scales 0, 1, 2, 3, 4, and 5. The number of Middle Blocks (MB in Fig. 2.3) is reduced from 16 to 8, as the extra discriminative power from those blocks is not needed. The input size is reduced from 512 px to 224 px to facilitate better computational performance, allowing for additional training and thus higher accuracy. Since the input resolution is reduced, the encoder is also modified to remove several down-sampling "max-pool" layers. The last contribution adds a 2-channel output to the decoder, allowing for both calving front masking and ice/ocean masking. Together, these changes reduce number of model parameters from 40M to 29M, while also increasing the overall accuracy.

Several techniques are used during the training of CALFIN-NN to improve its performance. First, a large set of training data is manually delineated (see Fig. S4), totalling 1541 Landsat and 232 Antarctic Sentinel 1A/B image/mask pairs, with the Antarctic data taken from the same training scenes used by Baumhoer et al. [2019]. Data augmentation is used to

increase the accuracy of the network by expanding the training set, which entails adding random amounts of flips, Gaussian noise, sharpening filters, rotations of up to 12°, crops, and scaling to the pre-processed training images. Through empirical testing, it is determined that excessive image padding, rotation, warping, and cropping of calving fronts to close to the image bounds result in sub-optimal performance. Another helpful technique is the use of test-time augmentations, wherein each image subset is cut into 9 overlapping 224x224 image windows and processed individually, before being reassembled into the final 256x256 output mask. This allows for multiple independent classifications of the central pixels, ensuring agreement and confidence in detected calving fronts. To increase accuracy, a custom loss function optimizes the binary cross entropy and Intersection-over-Union (see Eq. 2.1, Sect. 3.1) [Mannor et al., 2005]. This penalizes mismatches between calving front pixels in the predicted ($\mathbf{I_{cf}}$) and measured ($\hat{\mathbf{I}}_{\mathbf{cf}}$) image masks. Mismatched ice/ocean pixels in the predicted ($\mathbf{I_{io}}$) and measured ($\hat{\mathbf{I}}_{\mathbf{io}}$) image masks are less heavily weighted by an empirically chosen factor of $\alpha = 1/25$, as seen in the final loss function $\mathcal{L}$ in Eq. 2.2.

$$\mathcal{L}_{\mathcal{BI}}(\mathbf{I}, \hat{\mathbf{I}}) = -\mathbf{I}\log(\hat{\mathbf{I}}) - (1-\mathbf{I})\log(1-\hat{\mathbf{I}}) - \log\left(\frac{\mathbf{I} \cap \hat{\mathbf{I}}}{\mathbf{I} \cup \hat{\mathbf{I}}}\right) \tag{2.1}$$

$$\mathcal{L}(\mathbf{I_{cf}}, \hat{\mathbf{I}}_{\mathbf{cf}}, \mathbf{I_{io}}, \hat{\mathbf{I}}_{\mathbf{io}}) = \alpha\mathcal{L}_{\mathcal{BI}}(\mathbf{I_{io}}, \mathbf{I_{io}}) + (1-\alpha)\mathcal{L}_{\mathcal{BI}}(\mathbf{I_{cf}}, \hat{\mathbf{I}}_{\mathbf{cf}}) \tag{2.2}$$

After integrating these improvements, CALFIN-NN is trained for a total of 80 epochs, with 4000 batches per epoch, and 8 images per batch. Training is carried out on a K40 Nvidia Tesla GPU with 12GB of VRAM, with each epoch taking about 126 minutes to complete, and almost 1 week in total to obtain the optimal weights at epoch 65. Once trained, an NVIDIA GTX1060 with 6GB VRAM is used for the off-line data processing of the 20188 GeoTIFF subsets. The CALFIN algorithm takes about 3.5 days to process all of the subsets into calving fronts, excluding preprocessing, but including post-processing, as discussed in

the following section.

2.3 Post-Processing

At this stage, the 2-channel pixel mask output of CALFIN-NN is post-processed to extract the Shapefile data products (Fig. 2.4).

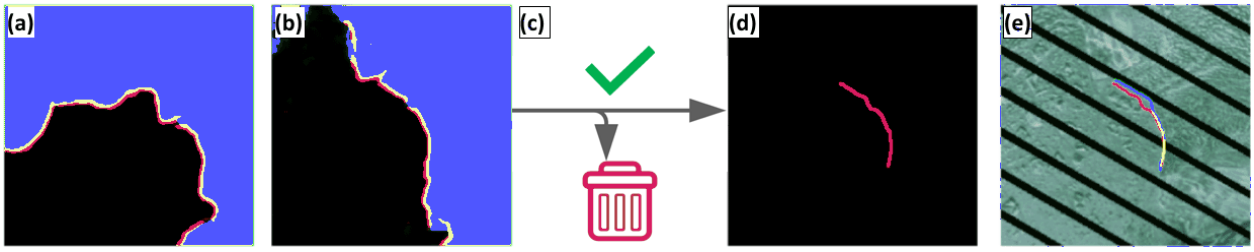

Figure 2.4: **Postprocessing Pipeline**: (a) First, get the processed image from CALFIN-NN. (b) Then, isolate and re-process each front. (c) Next, filter unconfident predictions. (d) Now, fit line and mask static coastline (see also Fig. 2.5). (e) Lastly, export and validate the Shapefile.

The first task in retrieving the correct coastline boundary is to transform the 2-channel pixel mask into a polyline data structure. At this point, the raw pixel mask may contain incorrect detections (false positives, Type I errors) and gaps (false negatives, Type II errors) due to the limitations of CALFIN-NN and its training regimen. In the absence of these errors, a polyline could be extracted from the pixel mask by finding the shortest path between all positively detected edge pixels in the pixel mask. However, the removal of such errors through standard computer vision techniques (such as such as through the successive applications of the dilation and erosion morphological operators) is not sufficient, introduces uncertainties in the output data, and fails to remove errors consistently in the general case. In light of this, the following approach is used to account for such errors during the polyline extraction process. This approach involves treating this problem as a subset of the path finding Orienteering Problem, or more specifically as a variant of the Tourist Trip Design Problem. This involves determining a path through a subset of given points with associated values that optimizes some cost function [Vansteenwegen and Oudheusden, 2007]. Within the context of this task,

the given set of points is the set of detected edge pixels, the subset of the given points is the path that corresponds to the correct coastline boundary, and the cost function is based on the distance between each pixel and its nearest neighbors.

First, each pixel in the pixel mask's 2nd channel (edge mask) to nodes in a graph. connecting the nearest neighboring nodes, then finding the single longest path in the graph's minimum spanning tree (MST) [Kruskal, 1956]. This path not only corresponds with the coastline edge, but also out-performs outputs from other contour finding algorithms by eliminating noise, errors, and gaps inherited from previous steps. Such gaps are given weights based on the negative exponential distances between nodes, which allows for connections if the joined paths are significantly longer than the gap itself. A visual example is given in Fig. 2.5a-d.

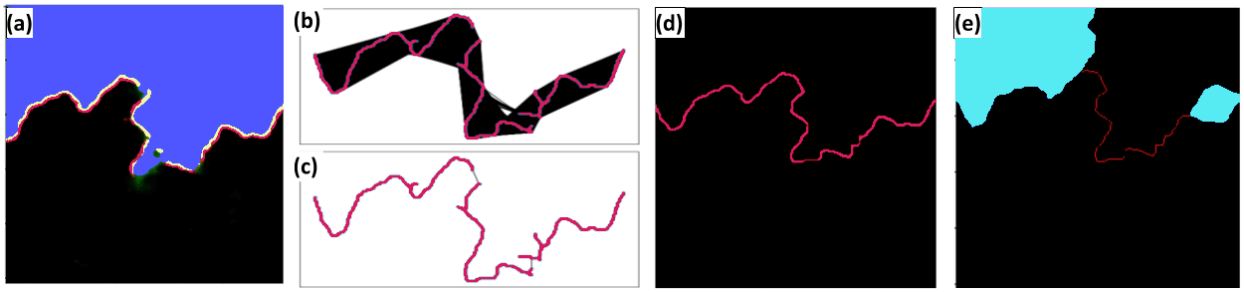

Figure 2.5: **Mask to Polyline Algorithm**: (a) First, extract the coastline mask (red/yellow) from the CALFIN-NN output. (b) Then create a graph, connecting each pixel (red) to 15% of its nearest neighbors with an edge (black). (c) Next, create an MST from the graph. (d) Now, extract the longest path from the MST. (e) Finally, mask the static coastline using the fjord boundaries (cyan) to extract the calving front.

Next, the calving front is isolated from the coastline polyline. Static masks of the average fjord boundaries are manually created for each basin using the image subsets and BedMachine v3 for reference [Morlighem et al., 2017]. By calculating the distance from each point in the coastline to the nearest fjord boundary pixel, then selecting the contiguous pixels which are the farthest from the fjord boundaries, the calving front can be isolated. The result of this is shown in Fig 2.5e.

Once each front is located, its bounding box is used to extract a higher resolution subset from the original image, and reprocessed. This innovation allows for increased spatial ac-

curacy when processing multiple fronts in large basins. After reprocessing, the nature of CALFIN-NN's 2-channel output as a confidence measure is exploited to filter out uncertain detections. Since the neural network assigns each pixel a value between 0 and 1 based on its perceived class, any deviation from these two values can used as a measure of uncertainty. The filtering method averages the deviation of the ice/ocean classification mask in a 5 pixel wide buffer around the calving front, and discards any fronts whose mean deviation exceeds an empirically chosen threshold of 0.125.

The last step is to export the polylines and the corresponding polygon as geo-referenced Shapefiles. First, the polylines are smoothed to eliminate noise artifacts inherited from previous steps, deviating no more than 1 pixel from the raw extracted coastline (see Appendix Fig. A2). Next, the smoothed polylines, fjord boundary mask, and land-ice/ocean masks are combined to create a polygonal ocean mask.

This is performed by overlaying the smooth polylines onto the fjord boundary mask, segmenting regions delineated by the polyline and fjord boundaries, setting all pixels within each region to the dominant class within said region, and finally vectoring the resulting binary land-ice/ocean masks into a polygonal Shapefile.

Optionally, manual verification of each output with the original GeoTIFF subset can be performed. This was done for all cases in this work to ensure the validity of the automated pipeline. This constrains the mean distance error to be <100 m, as covered in the following Chapter.

Chapter 3

Validation

Two methods are used to evaluate CALFIN. For the primary method, the error is estimated by calculating the Mean/Median Distance between predicted and manually delineated fronts (see Fig. 3.1a and Sect. 3.1). For the secondary method, the classification accuracy is calculated with the Intersection over Union metric (see Fig. 3.1b and Sect. 3.2). Additionally, the detection accuracy is evaluated, and the associated confusion matrix is provided (see Table 3.1 and Sect. 3.4). These metrics are evaluated on several validation sets, taken from existing studies as discussed in Sect. 1. These validation sets contain data that are excluded during model training. This prevents the models from memorizing data and skewing the accuracy assessment.

3.1 Error Estimation

The primary quality assessment method is the Mean Distance Error [Mohajerani et al., 2019; Zhang et al., 2019; Baumhoer et al., 2019]. Conceptually, this method resembles the numerical integration of the area between two curves, normalized by the average length of

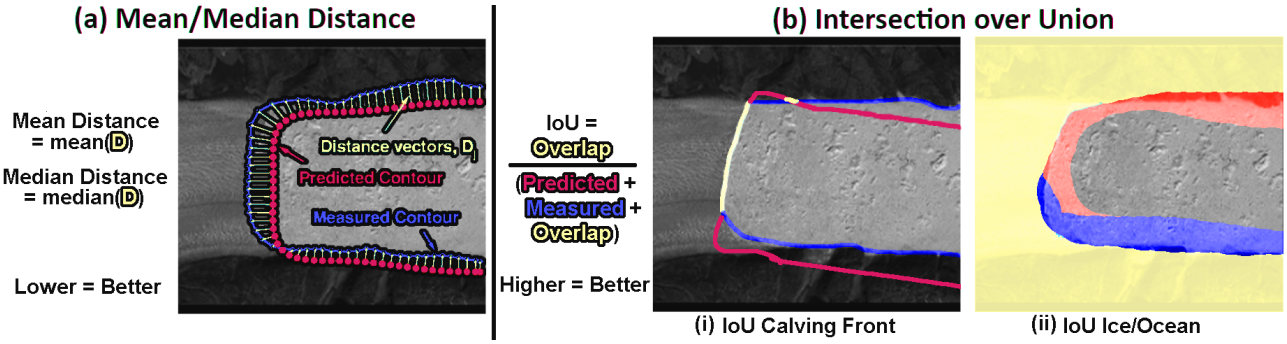

Figure 3.1: **Error Measures**: (a) A visual outline of Mean/Median Distance Error Estimation and (b) Classification Accuracy using Intersection over Union (IoU) for (i) the primary calving front, and (ii) the secondary ice/ocean mask, respectively.

the curves (see Fig. 3.1a). Also referred to as the Area over Front (A/F) in literature, this method can also be seen as a generalization of the method of transects along arbitrarily oriented fronts [Mohajerani et al., 2019; Baumhoer et al., 2019]. This metric is implemented by taking the mean/median of the distances between closest pixels in the predicted and manually delineated fronts. Note that pixel distance is biased to be inversely proportional to a network's input size, so the error in meters is also provided in the following analysis.

3.2 Classification Accuracy

The secondary quality assessment method calculates the Intersection over Union (IoU) [Baumhoer et al., 2019]. This metric evaluates the degree of overlap between the predicted and manually delineated masks of the calving front. It is calculated by dividing the number of pixels in the intersection of two masks over the number of pixels in the union of the two masks (see Fig. 3.1b). When calculating the IoU of 3 pixel wide edges, this measure is very strict: 1 pixel of difference results in a score of 0.5, and scores at or above that range are indicative of human levels of accuracy. When calculating the IoU of land-ice/ocean masks, this measure is less strict, and scores at or above 0.9 indicate human levels of accuracy.

3.3 Validation Results

The following subsections show tables with the above metrics for the associated validation sets, the values from the original studies, and a subset of the outputs of CALFIN-NN on each. The primary validation set, the CALFIN validation set (CALFIN-VS), consists of 162 images with clouds, illumination differences, ice mélange, and Landsat 7 Scanline Corrector Errors (L7SCEs). The CALFIN-VS contains data from 62 Greenlandic basins, including Helheim, which was specifically excluded from CALFIN's training set for validation purposes - as done by Mohajerani et al. [2019]. The CALFIN-VS ensures CALFIN-NN produces consistent results on new data, addressing concerns raised by Zhang et al. [2019] Sect. 7.3. To evaluate performance on Landsat 7 Scanline Corrector Errors, the validation subset CALFIN-VS-L7-only isolates images with L7SCEs, and the CALFIN-VS-L7-none excludes images with L7SCEs. To allow for comparisons between studies, CALFIN-NN's performance metrics on previous studies' validation sets are also shown, where appropriate. The sets include the 10 Landsat Helheim subsets used in Mohajerani et al. [2019] (M-VS), the 6 TerraSAR-X Jakobshavn subsets used in Zhang et al. [2019] (Z-VS), and 62 Sentinel-1 Antarctic basins taken from the 11 validation scenes used in Baumhoer et al. [2019] (B-VS). Note that the error metrics are still sensitive to how each study implements them, which are nevertheless reproduced and documented for comparison's sake. These concerns are also addressed in the comprehensive inter-model comparison, discussed in Sect. 4.2.2.

CALFIN-NN performs well on the CALFIN-VS (Fig. 3.2). The true mean distance error of the CALFIN dataset is calculated to be 86.76 ± 1.43 m with 95% confidence. When including only images with L7SCEs (CALFIN-VS-L7-only), the error is 91.93 m, showcasing CALFIN-NN's unique robustness to L7SCEs. Intuitively, excluding "difficult" images with L7SCEs in the validation set (CALFIN-VS-L7-none) decreases the error to 81.65 m. The median distance error is only 44.59 m, showing that only a few outliers contribute considerably to the mean. For full outputs, see Appendix Figs. A5-A8.

Validation Set	Model	Mean Distance	Median Distance	IoU Calving Front	IoU Ice/Ocean
CALFIN-VS	CALFIN-NN	2.25 px, 86.76 m	1.21 px, 44.59 m	0.4884	0.9793
CALFIN-VS-L7-none	CALFIN-NN	2.27 px, 81.65 m	1.16 px, 44.01 m	0.4880	0.9819
CALFIN-VS-L7-only	CALFIN-NN	2.22 px, 91.93 m	1.33 px, 49.24 m	0.4888	0.9766

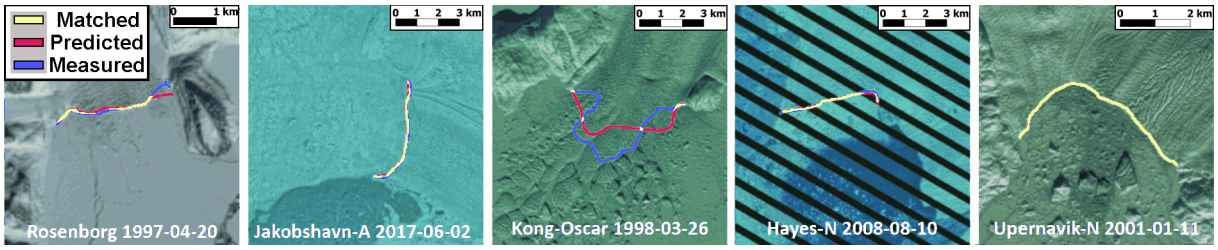

Figure 3.2: **CALFIN-VS Validation Output Results**: Yellow represents human (green) and machine (red) agreement on the front location. Note that the drop in mean pixel distance despite the increase in mean meter distance (and vice versa) comes from L7SCE images being reprocessed at lower sizes due to detection failures (see Fig. 2.4c), and pixel error bias being inversely related to input size (see Sect. 3.1).

Validation Set	Model	Mean Distance	Median Distance	IoU Calving Front	IoU Ice/Ocean
M-VS	CALFIN-NN	2.56 px, 97.72 m	2.55 px, 97.44 m	0.3332	N/A
M-VS	M-NN	1.97 px, 96.31 m	N/A	N/A	N/A

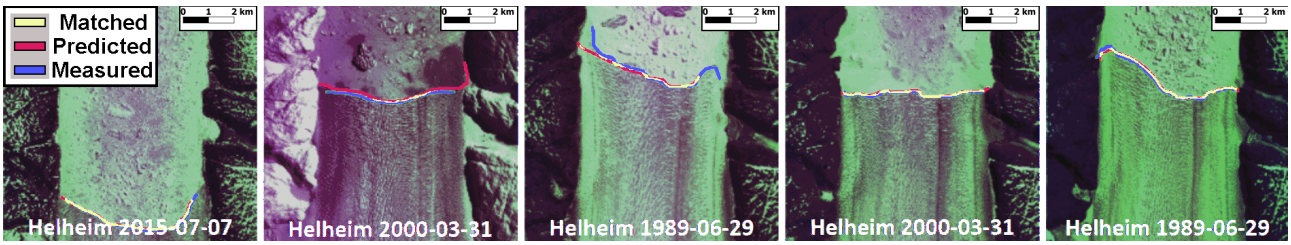

Figure 3.3: **M-VS Validation Output Results**: Note that CALFIN-NN has never trained on Helheim, but can still predict the front under different conditions and preprocessing methods. See Fig. S9. for full outputs.

CALFIN-NN performs well on the M-VS (Fig. 3.3). This demonstrates CALFIN-NN's ability to accurately process new data, which builds upon the Mohajerani et al. [2019] neural network

Validation Set	Model	Mean Distance	Median Distance	IoU Calving Front	IoU Ice/Ocean
Z-VS	CALFIN-NN	2.11 px, 115.24 m	1.65 px, 77.29 m	0.3832	0.9761
Z-VS	Z-NN	17.3 px, 104 m	N/A	N/A	N/A

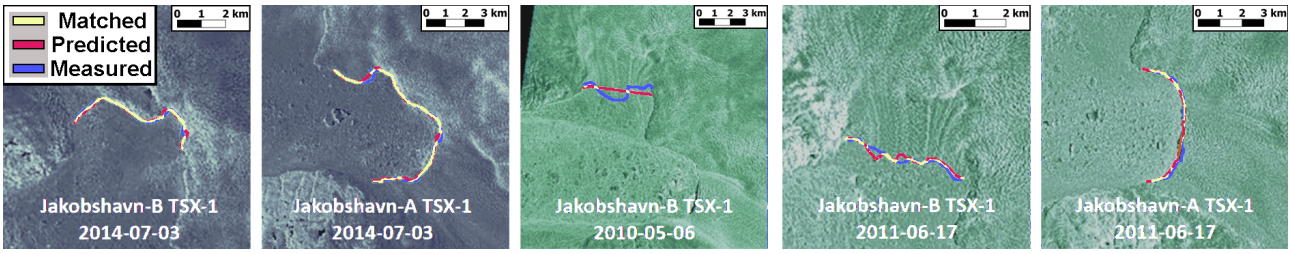

Figure 3.4: **Z-VS Validation Output Results**: CALFIN-NN works well on SAR data in addition to optical data. See Fig. S10. for full outputs.

Validation Set	Model	Mean Distance	Median Distance	IoU Calving Front	IoU Ice/Ocean
B-VS	CALFIN-NN	2.35 px, 330.63 m	0.74 px, 112.75 m	0.6451	0.9879
B-VS	B-NN	2.69 px, 108 m	N/A	N/A	0.905

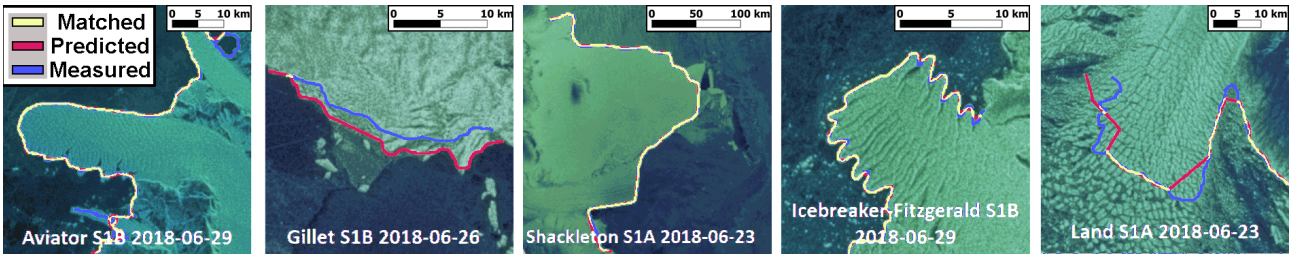

Figure 3.5: **B-VS Validation Output Results**: Similar to Z-NN, B-NN uses a high resolution input (768×768) relative to CALFIN-NN (224x224), which skews the mean pixel distance comparison in CALFIN-NN's favor. See Fig. S11-S12 for full outputs.

(M-NN). Note that M-NN implements distances errors differently, and omits ice/ocean masks from the evaluation. This differences are further explored in the Sect. 4.2.2 model inter-comparison.

CALFIN-NN performs competitively on the Z-VS (Fig. 3.4). It achieves a similar mean meter distance (115.24 m vs. 104 m) despite being constrained to using lower resolution

TerraSAR-X data. Note though that the Zhang et al. [2019] neural network (Z-NN) uses higher resolution input data (960×720) compared to CALFIN-NN (224x224), which skews the mean pixel distance comparison, where CALFIN-NN performs better (2.11 px vs. 17.3 px). Another source of skew comes from CALFIN-NN confidence filtering, as only 8 of 12 fronts in the set are confidently detected (see Sect. 3.4). Increasing CALFIN-NN's input resolution and training on higher resolution SAR data may enable CALFIN-NN to detect more fronts with greater accuracy.

CALFIN-NN performs sub-par on the B-VS (Fig. 3.5). When comparing the mean distance error with the Baumhoer et al. [2019] equivalent Area over Front (A/F) error, the Baumhoer et al. [2019] neural network (B-NN) outperforms CALFIN-NN (330.63 m vs 108 m). Note that the easily detected static coastlines are masked out, raising the relative error, and negatively impacting CALFIN-NN's performance on this metric. When comparing metrics that isolate the calving front, the absolute median distance error is calculated (achieving 112.75 m) whereas Baumhoer et al. [2019] uses signed median distance error (achieving 0 m), which is not directly comparable in this context, and thus omitted. Currently, the error is affected by kilometer-range deviations in very large domains like Voyeykov Ice Shelf, and differences in sea-ice mélange as seen along the Gillet and Wordie Ice Shelves, which would be consistent with findings in Baumhoer et al. [2019] Sect. 5.2. After excluding such outliers, fronts are detected in 55 out of 62 domains (88.71%), achieving median distance errors of 0.95 px (127.87 m). Intensive retraining on ice shelves may be required for CALFIN-NN to improve.

3.4 Detection Accuracy

Lastly, CALFIN-NN is shown to automatically filter images that do not have detectable calving fronts. To verify this, 13 images are included in the CALFIN-VS which do not contain

calving fronts discernible to the human eye. The true positive (TP), true negative (TN), false positive (FP), and false negative (FN) rates are computed for the entire 162 image CALFIN-VS, and the associated confusion matrix is shown in Table 3.1. Note that CALFIN-NN does not output any false positives on the CALFIN-VS. While this ensures accurate fronts are output rather than incorrect fronts, this filtering behavior removes potentially large errors, and must be accounted for when comparing errors across other sets.

Table 3.1: **Confusion Matrix**: CALFIN-NN misses fronts in 8 of 149 valid CALFIN-VS images, but this trade-off is acceptable.

		Front Detected?	
		Yes	No
Front Detectable?	Yes	TP = 141/149 (94.63%)	FN = 8/149 (5.76%)
	No	FP = 0/13 (0.00%)	TN = 13/13 (100.00%)

Chapter 4

Results and Discussion

The code implementation of the CALFIN method is released, along with its associated calving front data products as described in the following section, for use within the scientific community. The CALFIN dataset spans 66 Greenlandic basins, over the period Sept. 1972 - June 2019. It consists of over 1500 manual delineations and 22,678 total calving fronts. Two levels of CALFIN data products are provided. The Level 0 products include the Shapefile domains used for subsetting, the neural network training image/mask pairs, the fjord boundary masks, the full Landsat scene ID list, and the quality assurance images for validation purposes. The use cases of Level 0 products may include studies of reproducibility, validation, or training new neural networks. The Level 1 products include the calving front polyline and polygon Shapefiles. The polyline product consists of the isolated, refined, georeferenced, and verified calving fronts for each domain. The polygon product consists of an ocean mask bounded by the domain subset, the fjord boundaries, and the calving front(s), for each domain. Both of the Shapefiles share a common metadata feature schema (see Table A2 and the following Sect. 4.1) derived from the MEaSUREs Glacial Termini Dataset [Moon and Joughin, 2008; Joughin et al., 2015] and TermPicks [Goliber et al., 2021], and names are derived from [Bjørk et al., 2015]. These products can be found via these links to Github

and DataDryad [Cheng et al., 2020].

4.1 Information Available From Our Method

Each glacial feature generated by the CALFIN methodology shares a common metadata feature schema that provides useful information for end-users of the CALFIN Level 1 data products. These data products use the NSIDC Sea Ice Polar Stereographic North projection system (EPSG:3413), and the information associated with each feature allows for the verification of the CALFIN results (by providing the original source ImageIDs, the author, and quality flags, among other parameters). The full schema is as follows.

Glacier ID: The GlacierID provides a unique numerical id to identify glaciers with multiple or disputed common names. The IDs are assigned to major glaciers beginning with Jakobshavn Isbrae in Central West Greenland, beginning at 1 and increasing to 238 in a counter-clockwise order around Greenland's coast, as detailed in [Moon and Joughin, 2008; Joughin et al., 2015]. Minor glaciers not designated in [Moon and Joughin, 2008; Joughin et al., 2015] are given new ids beginning at 238 and increasing to 246 in an unordered fashion consistent with the TermPicks glacier ID scheme [Goliber et al., 2021]. In addition to resolving the identification of glaciers with multiple or disputed common names, unique GlacierIDs help track the converging and diverging evolution of multiple branches within a single glacial basin, allowing for easier and more consistent long term studies of complex glacial systems.

Center X, Center Y, Latitude and Longitude: The CenterX and CenterY parameters provide the X/Y coordinates for the centroid point of each polyline or polygonal feature. Similarly, the Latitude and Longitude parameters corresponding to the centroid point is also provided. The CenterX/CenterY parameters are given in the NSIDC Sea Ice Polar Stereo-

graphic North projection system (EPSG:3413), and the Latitude/Longitude parameters are given in the WGS84 (World Geodetic System 1984) coordinate system (EPSG:4326). These centroid point parameters are provided for applications where only a rough approximation of the glacial feature positions are required.

Quality Flag: The Quality Flag parameter, or QualFlag, identifies the method and potential sources of error associated with individual data features. The flag consists of a 2 digit bit mask, the first digit specifying the method of feature extraction, and the second digit specifying which type of potential error that is present in the feature source data. As with other parameters in this dataset, this schema is chosen to be compatible with existing metadata standards [Moon and Joughin, 2008; Goliber et al., 2021], and anticipates future developments by leaving room for other flag values. Flags values beginning with 0 are manually digitized, which is the case for all features extracted from the training and validation images re-purposed from the development of the CALFIN-NN. Flag values beginning with 1 are automatically digitized, as is the case with all other features in the dataset. Flag values ending in 3 specify features that were derived from source images containing Landsat 7 Scan-line Corrector Errors (L7SCEs). Flag values ending in 0 specify features that were derived from source images no L7SCEs. Flag values ending in other values (1, 2, 4-9) are not defined within the context of this dataset, but are reserved for use in existing and future glacial feature datasets. Thus the flags themselves take on 4 discrete values, where 00 identifies a feature that was manually digitized, 03 identifies a feature that was manually digitized from source images with L7SCEs, 10 identifies a features that was automatically digitized, and 13 identifies a feature that automatically digitized from source images with L7SCEs.

Satellite: The Satellite parameter provides the original sensor or satellite that produced the image from which the glacial feature was extracted. This parameter is automatically

taken from the associated ImageID parameter, and is useful for identifying potential systemic issues associated with certain image sensors or satellites. This parameter may take on a variety of values that conform the format "LXSS" where L represents Landsat, X, represents the sensor, and SS represents the two-digit number assigned to the satellite. Within this metadata schema, 07 represents the Landsat 7 ETM+ sensor, and other possible values for "X", the sensor are: "C"=OLI/TIRS combined (Operational Land Imager/Thermal InfraRed Sensor), "O"=OLI-only, "T"=TIRS-only, "E"=ETM+ (Extended Thermal Mapper Plus), "T"="TM" (Thermal Mapper), and "M"="MSS" (MultiSpectral Scanner).

Date: The Date parameter represents the acquisition time for the image from which the feature is extracted. This parameter is also automatically taken from the associated ImageID parameter. The Date format is "YYYY-MM-DD", where YYYY (Year), MM (month), and DD (day) are integers, and Dates ranging from 1972-09-06 to 2019-06-25.

Image ID: The ImageID parameter refers to the original source image identifier from which the feature is extracted. Since the original images are not provided as part of the data products, this parameter provides the necessary information for future studies to verify and validate the extracted glacial features.

Greenlandic Name, Official Name, Alternative Name, Reference Name: These common name parameters provide the associated with. Not all features or glacier have The Greenlandic Name, abbreviated "GrnlndcN", is the The Official Name, abbreviated "OfficialN", Greenlandic and Official Names are derived from [Bjørk et al., 2015]. The Alternative Name, abbreviated "AltName", The Reference Name, abbreviated "RefName", is

Author: Lastly, the author name is provided in conformance to metadata standards. In this case, the author name takes the format of LastName_FirstInitial, and the only associated value within the context of this dataset is "Cheng_D". This parameter enables the tracking of features from multiple potential sources by end users of this dataset.

4.2 Comparison with Existing Works

4.2.1 CALFIN vs. Calving Front Datasets ESA-CCI, PROMICE, and MEaSUREs

With the new data available to use in the CALFIN dataset, it is possible to explore seasonal trends across the Greenland Ice Sheet, and validate a subset of 10 high discharge basins of interest against existing ESA-CCI, MEaSUREs, and PROMICE data products [ENVEO, 2017; Joughin et al., 2015; Andersen et al., 2019]. Fig 4.1 shows the high temporal resolution and spatial accuracy of the CALFIN data product alongside corresponding available data products from 1972-2019. For Joughin et al. [2015], if a date range is given, the same relative change at both start and end dates [Moon and Joughin, 2008] is plotted. For Andersen et al. [2019], August 15th is used as the "end-of-melt-season" date of delineation, as the date is otherwise not specified in the provided data. The advance and retreat of the calving front along the basin centerlines is relative to their earliest positions. Note the large improvement in temporal/seasonal coverage and the general agreement of CALFIN with existing data products. Note also that the discrepancies such as that during 2005-2009 in Jakobshavn (Fig. 4.1e) mostly stem from a lack of winter coverage during Landsat's optical blackout period. Additional outliers in Kong Oscar (Fig. 4.1g) stem from the somewhat arbitrary delineation of the ice tongue front position. Kangiata Nunaata (Fig. 4.1j) suffers from both

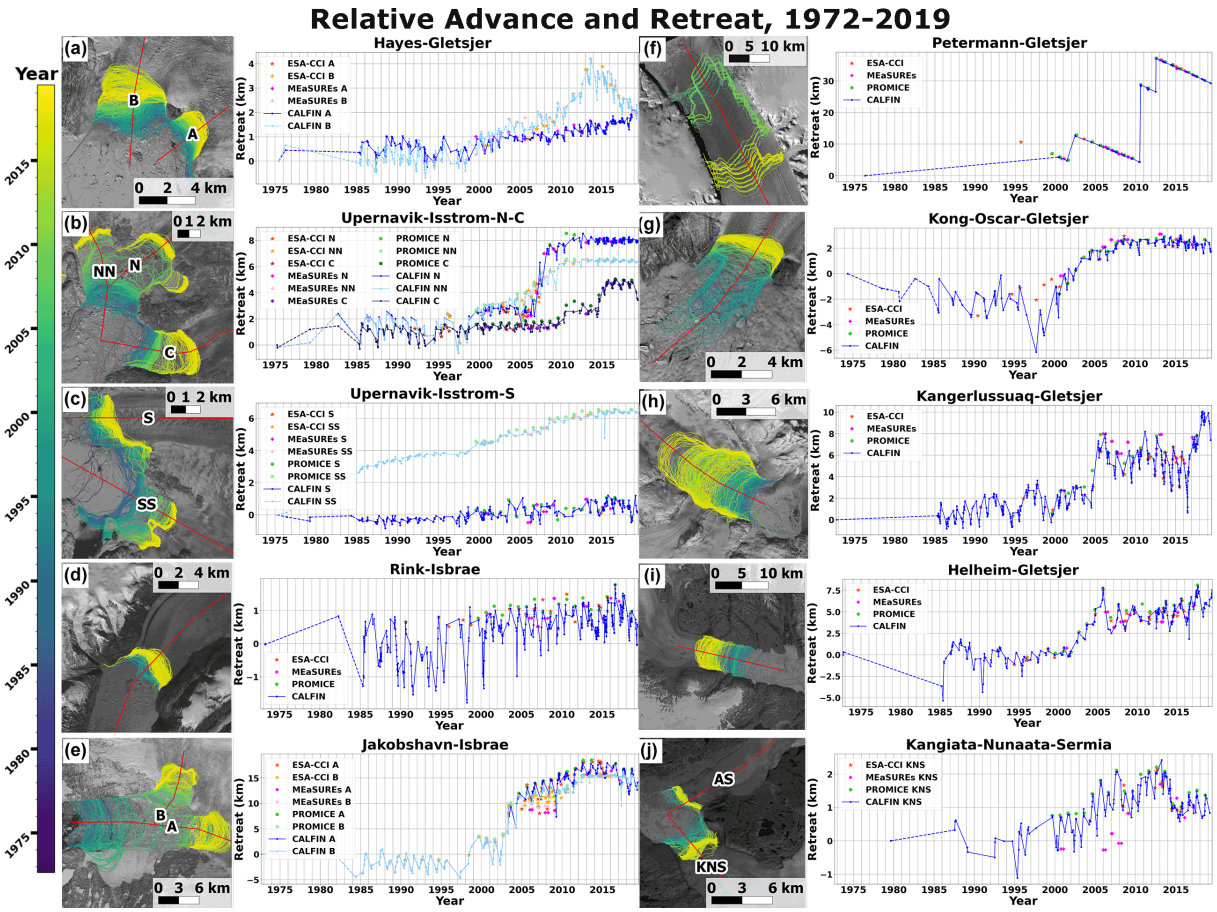

Figure 4.1: **Terminus Advance and Retreat Over Time**. (a-j) Basin setup (left) and graph (right) for 10 high discharge basins. Positive length change represents retreat relative to the earliest position along the centerlines in red. Note the seasonal variations captured by CALFIN, in blue. Time series for other studies span 1990-2016 (ESA-CCI), 2000-2017 (MEaSUREs), and 1999-2019 (PROMICE). Note the seasonal variations shown by the solid lines, and the dotted lines from 1972-1985 that indicate a lack of such seasonal observations. Also note that the vertical axis scaling is applied differently for each graph to highlight seasonal trends.

of the aforementioned effects, but otherwise shows the same general agreement with existing datasets from 2000 onwards.

Additionally, Fig. 4.2 shows the regional mean advance and retreat change, alongside the mean for the entirety of Greenland covered by the CALFIN dataset. Supplementary to the above, Fig. 4.2 shows similar the relationship between the 320-390 Gigatons of water/ice mass discharged per year, versus the calving front changes, as seen in King et al. [2020].

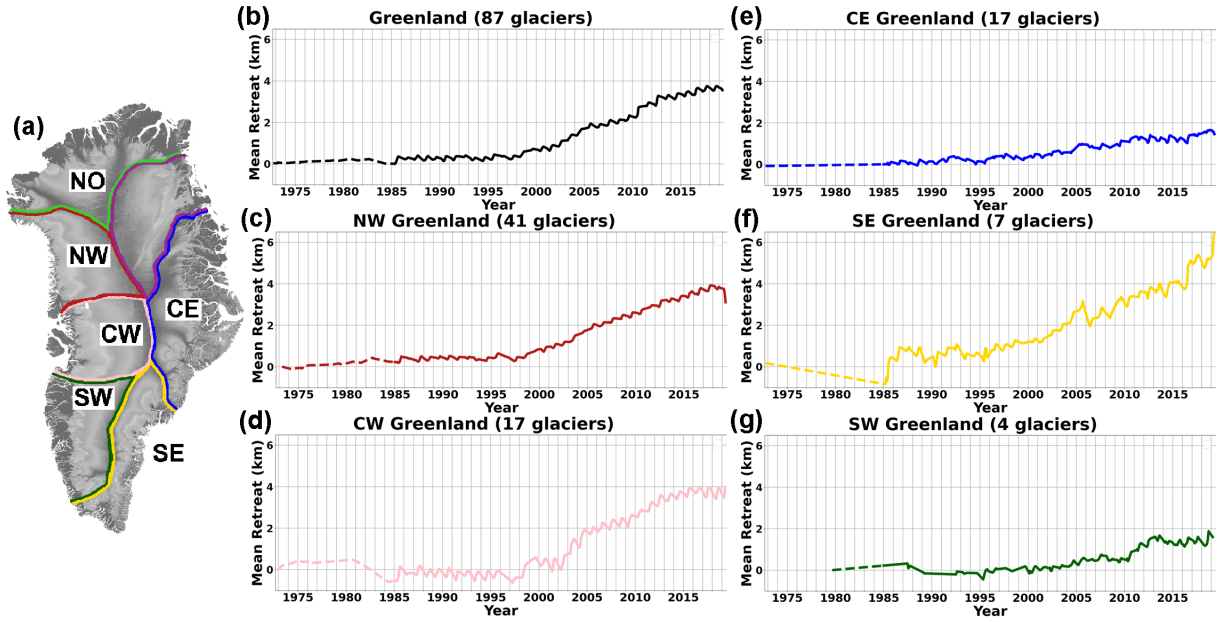

Figure 4.2: **Regional Terminus Advance and Retreat Over Time**. (a) Regional delineations (left) and terminus position graphs (right) for Greenland (b), as well as the northwestern (c), central western (d), central eastern (e), southeastern (f), and southwestern (g) regions. Note that the total Greenland mean advance and retreat is unadjusted, and dominated by the trend lines of numerous smaller glaciers in CW and NW Greenland. Note that branches in the 66 studied basins are independently counted, for a total of 87 glaciers.

Contributions from NW Greenland influence the overall trend the most, due to the presence of many small glaciers/branches in the region. Note that the mean for Greenland in Fig. 4.2 also includes contributions from Petermann, which is visible in the summers of 2010 and 2012. Across both figures, shared regional trends are visible across NW and CW Greenland, which both show relative stability before 2000, followed by steady retreat up until 2017-2018. CE and SE Greenland also share a similar but less pronounced retreat, showing an accelerating retreat beginning around 1995. These regional trends are less visible in SW Greenland, which is dominated by Narsap Sermia's retreat from 2010-2013. Overall, these regional trends generally agree with studies such as Wood et al. [2021] and King et al. [2020], contributing additional support for the CALFIN method and data.

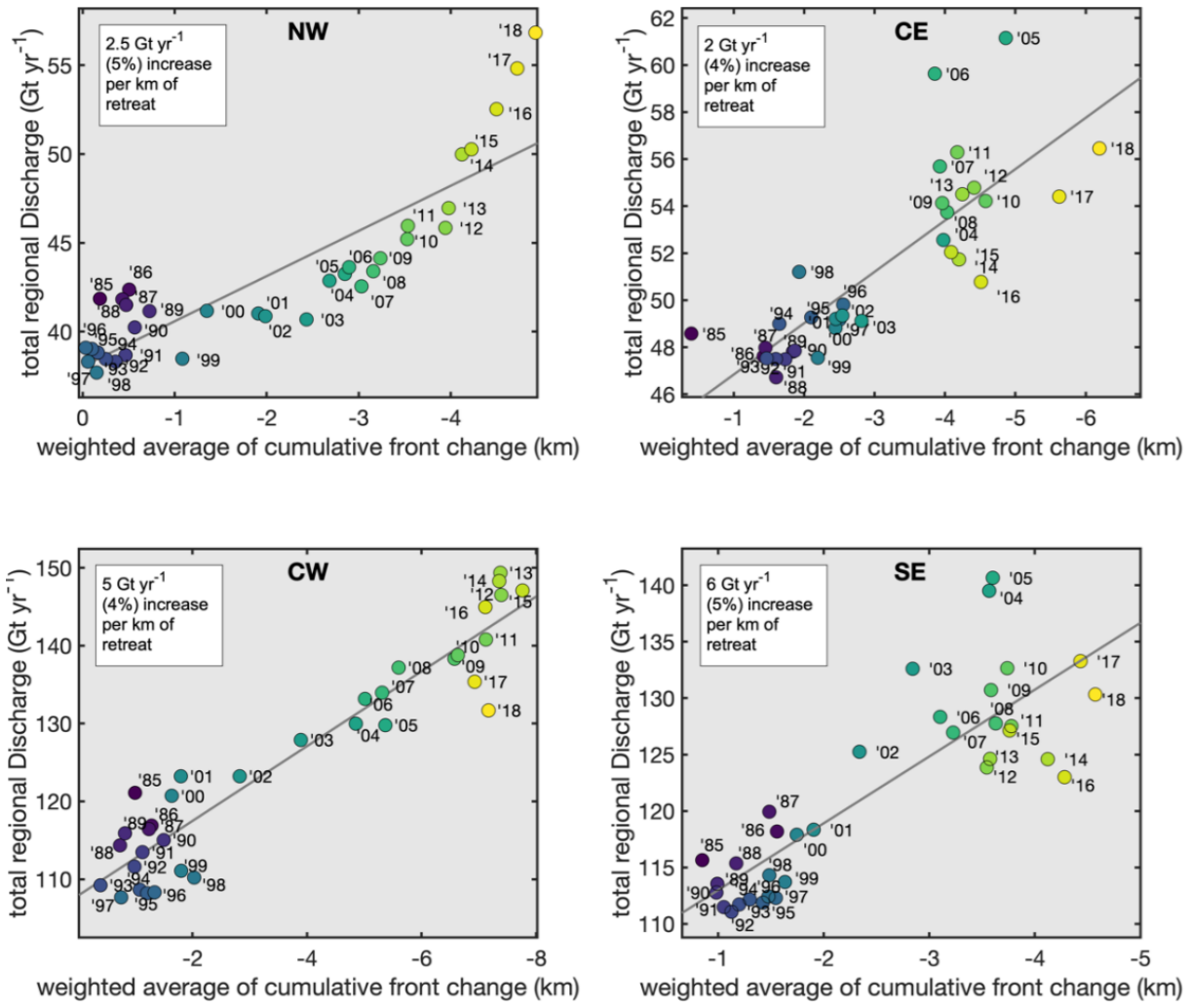

Figure 4.3: **Relations between Regional Discharge Volume and Terminus Advance and Retreat Over Time**. Regional graphs of water discharged mass (in Gigatons/year) versus calving front change, with a line of best fit plotted showing the clear relationship between the two metrics. Each data point represents the average annual values of all glaciers in each region, weighted by size. Derived from King et al. [2020].

4.2.2 Neural Network Architectural Comparison

To reinforce the validity of the methodology, and address the shortcomings of different error metric comparisons (as discussed in Sect. 3), a comprehensive inter-model comparison is conducted between CALFIN-NN and the model developed by Mohajerani et al. [2019] (M-NN). This experiment seeks to understand how both models perform, holding all other variables constant. In particular, this experiment seeks to determine if the M-NN model,

and by extension other UNet models, perform on par with the CALFIN-NN model, given the same training data. This task involves retraining the M-NN on CALFIN training data, and comparing its performance against CALFIN-NN using a shared validation set. For the fairest results, only images without L7SCEs are evaluated in this validation set - CALFIN-VS-L7-none - which is within the known capabilities of the M-NN. Furthermore, the same pre- and post-processing is applied to both models.

Table 4.1: **Model Inter-comparison Error Table**: Metrics for the CALFIN-NN and M-NN models on all non-Landsat 7 test images in the CALFIN validation set.

Validation Set	Training Set	Model	Mean Distance	Median Distance	IoU Front	IoU Ice/Ocean
CALFIN-VS-L7-none	CALFIN	CALFIN-NN	2.27 px, 81.65 m	1.16 px, 44.01 m	0.4880	0.9819
CALFIN-VS-L7-none	CALFIN	M-NN	4.45 px, 201.35 m	1.25 px, 50.52 m	0.4935	0.9699

Across all non-Landsat 7 test images in the CALFIN validation set, CALFIN-NN attains a 2.27 pixel (81.65 meter) mean distance between the predicted and the manually delineated fronts. This exceeds the level of accuracy achieved by the model from Mohajerani et al. [2019], which after retraining on CALFIN training data, is 4.45 pixels (201.35 meters). Note again that Landsat 7 images were excluded during reevaluation for the M-NN. This supports the findings that the CALFIN-NN architecture is an improvement over existing UNet models.

With this added context, the validation table is reproduced from Ch. 3, Fig. 3.3, and the error analysis is continued below. To reemphasize the differences in mean distance error calculation between different studies, Mohajerani et al. [2019] begins by breaking each predicted front to 1000 smaller segments within a small buffer from the fjord walls and calculating the mean deviation between the segments of the predicted and manually delineated fronts. The method begins by averaging the mean distance between each pixel of the predicted front and the closest pixel of the manually delineated front as detailed in Ch. 3.1. While the line-segment methodology of Mohajerani et al. [2019] provides a stricter estimate by enforc-

ing close agreement between corresponding front segments, the CALFIN method allows for non-aligned evaluation of the mean distance error. Although both implementations quantify the differences between the lines, the differences in implementation should still be considered when evaluating the comparison below.

Table 4.2: **M-VS Validation Output Results**: Accuracy and error metrics for the CALFIN-NN and the M-NN models on the M-VS. Again, some metrics are not provided by Mohajerani et al. [2019], so they are omitted from this table.

Validation Set	Training Set	Model	Mean Distance	Median Distance	IoU Front	IoU Ice/Ocean
M-VS	CALFIN	CALFIN-NN	2.56 px, 97.72 m	2.55 px, 97.44 m	0.3332	N/A
M-VS	Mohajerani	M-NN	1.97 px, 96.31 m	N/A	N/A	N/A

Across all 10 test images in the M-VS, CALFIN-NN attains a 2.56 pixel (97.72 meter) mean distance between the predicted and the manually delineated fronts. This approaches the level of accuracy achieved in our work, which is 1.97 pixels (96.31 meters). This supports the findings that the CALFIN-NN architecture generalizes to new data well. Note that CALFIN-NN's larger network size requires additional training data to avoid over-fitting, or memorizing, the training data, which could explain the slightly lesser accuracy when compared to the M-NN. In summary, this comprehensive model inter-comparison supports the hypothesis that the CALFIN-NN model improves on existing studies and is generalizing well.

4.2.3 Inter-author Data Comparison

Dervied from: Goliber, S., Black, T., Catania, G., Lea, J. M., Olsen, H., Cheng, D., Bevan, S., Bjørk, A., Bunce, C., Brough, S., Carr, J. R., Cowton, T., Gardner, A., Fahrner, D., Hill, E., Joughin, I., Korsgaard, N., Luckman, A., Moon, T., Murray, T., Sole, A., Wood, M., and Zhang, E.: TermPicks: A century of Greenland glacier terminus data for use in machine learning applications, The Cryosphere Discuss. [preprint], https://doi.org/10.5194/tc-2021-311, in review, 2021.

To further validate this work, an inter-author comparison is performed between CALFIN and all publicly available manually picked glacial calving front positional data, as listed in Table 4.3. This error analysis is carried out by comparing the maximum distances between co-temporal data for each permutation of dataset author pairs. Quantitatively, CALFIN contributes 22,678 out of 39,060, or 58%, of publicly available glacial calving front delineations, which means that it provides more data than all known existing datasets of calving fronts combined. Qualitatively, CALFIN contributes data within reasonable error margins, in particular when considering the large inter-author variance between existing calving front delineations as seen in Fig. 4.4. Large inter-author discrepancies, particularly between CALFIN and Hill et al. [2017, 2018], is primarily explained by the latter's focus on Northern Greenlandic glaciers with large ice tongues and crevasses (see Figure 1.2b/c) that make the determination of a calving front difficult. Notably, the overall median error between all inter-author pairs is 107 meters, which is comparable to the mean error obtained by CALFIN on evaluated validation sets. Since the average error of CALFIN with respect to other human generated datasets, it follows that CALFIN is a viable source of glacial calving front data for use within the scientific community.

Published Source	Spatial Coverage	Date Range	Resolution	Author Key
Andersen et al. [2019]	GrIS wide; n =47	1999-2018	Annual	PROMICE
Bevan et al. [2012]	GrIS wide; n = 14	1985-2011	Sub-annual	Bevan
Bevan et al. [2019]	Kangerlussuaq; n = 1	1985-2018	Sub-annual	Bevan
Bjørk et al. [2012]	SE GrIS, n =132	1931-2010	Sub-decadal	Bjork
Black and Joughin [2021]	NW GrIS; n = 87	1972-2021	Annual	Black
Brough et al. [2019]	Kangerlussuaq, n = 1	2013-2018	Sub-annual	Brough
Bunce et al. [2018]	NW and SE; n = 276	2000-2015	Annual	Bunce
Carr et al. [2013]	NW GrIS; n = 10	1976-2012	Decadal to monthly	Carr
Carr et al. [2017]	GrIS Wide; n = 273	1992-2010	Decadal	Carr
Carr et al. [2015]	Humboldt ; n = 1	1975-2012	Sub-decadal	Carr
Catania et al. [2018]	CW GrIS; n = 15	1965-2018	Sub-annual	Catania
Cheng et al. [2021]	GrIS wide; n = 65	1972-2019	Sub-annual	Cheng (CALFIN)
Cowton et al. [2018]	E GrIS; n = 10	1993–2012	Sub-annual	Sole
Fahrner et al. [2021]	GrIS wide; n = 224	1984–2017	Annual	Fahrner
Hill et al. [2017]	N GrIS; n = 21	1916-2015	Annual	Hill
Hill et al. [2018]	N GrIS; n = 18	1948-2015	Annual	Hill
Korsgaard [2021]	GrIS Wide; n = 452	1978–1987	Annual	Korsgaard
Moon and Joughin [2008]	GrIS wide; n = 203	1992-2007	Sub-decadal	Moon
Murray et al. [2015]	GrIS wide; n = 199	2000-2010	Sub-annual	Murray
Raup et al. [2007]	GrIS wide; n = 28	1990-2016	Sub-annual	ESA
Goliber et al. [2021]	E and W GrIS; n = 13	1985-2019	Sub-annual	TermPicks
Wood et al. [2021]	GrIS wide, n = 226	1992-2017	Annual	Wood
Zhang et al. [2019]	Helheim, Jakob., and Kanger.; n = 3	2009-2015	Sub-annual	Zhang

Table 4.3: Existing Sources for Calving Fronts. Spatial coverage describes the number of glaciers and name/region(s) of the traces. Date range are the years covered by the data set. Resolution is the temporal resolution; Annual is approximately one delineation per year, sub-annual is more than one trace per year, decadal is approximately one trace every ten years, sub-decadal is more than one trace every 10 years, but not each year. Method is the tracing method used by the author to digitize the terminus. The Author key is the label given to that data set in the inter-author error table.

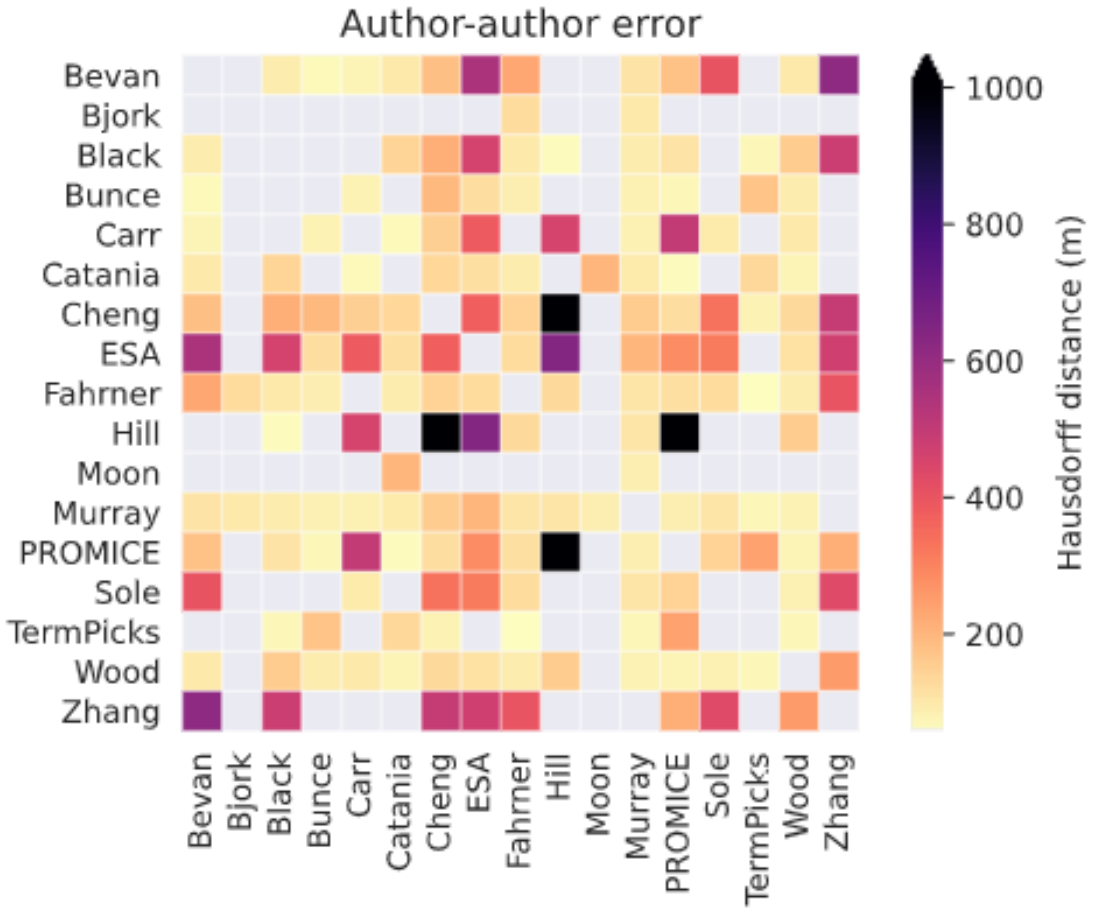

Figure 4.4: **Median Inter-author Error**. The greatest median error (7,350 m) is between Cheng (CALFIN) and Hill. The average median error (107 m) is comparable to CALFIN's performance on evaluated validation sets.

Chapter 5

Future Directions and Conclusion

Overall, the goal of automatically delineating calving fronts from satellite imagery is accomplished. The CALFIN method uses the cutting-edge in deep learning architectures, allowing for robustness to minor cloud cover, Landsat 7 Scanline Corrector Errors, and illumination changes. The method is validated through a comprehensive data intercomparison with existing studies, and the results deviate by on average 86.76 ± 1.43 meters from the measured fronts. Regional trends show larger than average absolute retreat in SE Greenland, and new sub-seasonal trends are available for further investigation with the release of the 22,678 calving front lines generated across 66 Greenlandic glaciers. Future work may entail accuracy improvements, expansion of included domains, usage of SAR data sources, and near-real time data products. Within the community, the benefits of standardized training, validation sets, and outputs/metadata are anticipated. The community's development of new automated extraction studies, such as grounding line delineation, iceberg tracking, and sea ice mélange measurements, is also anticipated. A key takeaway is the maturation of neural networks for automated calving front detection. Specifically, a well trained network now approaches human levels of accuracy in picking arbitrary glacial calving fronts. This reinforces existing studies on the viability of the methodology, and paves the way for applications on other data

processing tasks. Ultimately, this work showcases the state-of-the-art in automated calving front detection, and provides a new database of glacial termini positions for the cryosphere community.

Bibliography

Andersen, J. K., Fausto, R. S., Hansen, K., Box, J. E., Andersen, S. B., Ahlstrøm, A. P., van As, D., Citterio, M., Colgan, W., Karlsson, N. B., Kjeldsen, K. K., Korsgaard, N. J., Larsen, S. H., Mankoff, K. D., Pedersen, A. Ø., Shields, C. L., Solgaard, A., and Vandecrux, B. (2019). Update of annual calving front lines for 47 marine terminating outlet glaciers in greenland (1999–2018). *GEUS Bulletin*, 43.

Andersen, M., Stenseng, L., Skourup, H., Colgan, W., Khan, S., Kristensen, S., Andersen, S., Box, J., Ahlstrøm, A., Fettweis, X., and Forsberg, R. (2015). Basin-scale partitioning of greenland ice sheet mass balance components (2007–2011). *Earth and Planetary Science Letters*, 409:89 – 95.

Baumhoer, C. A., Dietz, A. J., Kneisel, C., and Kuenzer, C. (2019). Automated extraction of antarctic glacier and ice shelf fronts from sentinel-1 imagery using deep learning. *Remote Sensing*, 11(21):2529.

Bevan, S. L., Luckman, A. J., Benn, D. I., Cowton, T., and Todd, J. (2019). Impact of warming shelf waters on ice mélange and terminus retreat at a large SE Greenland glacier. *The Cryosphere*, 13(9):2303–2315.

Bevan, S. L., Luckman, A. J., and Murray, T. (2012). Glacier dynamics over the last quarter of a century at Helheim, Kangerdlugssuaq and 14 other major Greenland outlet glaciers. *The Cryosphere*, 6(5):923 – 937.

Bjørk, A. A., Kruse, L. M., and Michaelsen, P. B. (2015). Brief communication: Getting greenland's glaciers right – a new data set of all official greenlandic glacier names. *The Cryosphere*, 9(6):2215–2218.

Bjørk, A. A., Kjær, K. H., Korsgaard, N. J., Khan, S. A., Kjellerup, K. K., Andresen, C. S., Box, J. E., Larsen, N. K., and Funder, S. (2012). An aerial view of 80 years of climate-related glacier fluctuations in southeast Greenland. *Nature Geoscience*, 5(6):427 – 432.

Black, T. E. and Joughin, I. (in review; 2021). Multi-decadal retreat of marine-terminating outlet glaciers in northwest and central-west greenland.

Brough, S., Carr, J. R., Ross, N., and Lea, J. M. (2019). Exceptional Retreat of Kangerlussuaq Glacier, East Greenland, Between 2016 and 2018. *Frontiers in Earth Science*, 7(123):123.

Bunce, C., Carr, J. R., Nienow, P. W., Ross, N., and Killick, R. (2018). Ice front change of marine-terminating outlet glaciers in northwest and southeast greenland during the 21st century. *Journal of Glaciology*, 64(246):523–535.

Carr, J. R., Stokes, C. R., and Vieli, A. (2017). Threefold increase in marine-terminating outlet glacier retreat rates across the atlantic arctic: 1992–2010. *Annals of Glaciology*, 58(74):72–91.

Carr, J. R., Vieli, A., and Stokes, C. R. (2013). Influence of sea ice decline, atmospheric warming, and glacier width on marine-terminating outlet glacier behavior in northwest Greenland at seasonal to interannual timescales. *Journal of Geophysical Research: Earth Surface*, 118(3):1210 – 1226.

Carr, J. R., Vieli, A., Stokes, C. R., Jamieson, S. S. R., Palmer, S. J., Christoffersen, P., Dowdeswell, J. A., Nick, F. M., Blankenship, D. D., and Young, D. A. (2015). Basal topographic controls on rapid retreat of Humboldt Glacier, northern Greenland. *Journal of Glaciology*, 61(225):137 – 150.

Catania, G. A., Stearns, L. A., Moon, T. A., Enderlin, E. M., and Jackson, R. H. (2020). Future evolution of greenland's marine-terminating outlet glaciers. *Journal of Geophysical Research: Earth Surface*, 125(2):e2018JF004873.

Catania, G. A., Stearns, L. A., Sutherland, D. A., Fried, M. J., Bartholomaus, T. C., Morlighem, M., Shroyer, E., and Nash, J. (2018). Geometric controls on tidewater glacier retreat in central western greenland. *Journal of Geophysical Research: Earth Surface*, 123(8):2024–2038.

Chen, L., Zhu, Y., Papandreou, G., Schroff, F., and Adam, H. (2018). Encoder-decoder with atrous separable convolution for semantic image segmentation. *European Conference on Computer Vision*, pages 801–818.

Chen, X., Zhang, X., Church, J. A., Watson, C. S., King, M. A., Monselesan, D., Legresy, B., and Harig, C. (2017). The increasing rate of global mean sea-level rise during 1993–2014. *Nature Climate Change*, 7(7):492–495. Bandiera_abtest: a Cg_type: Nature Research Journals Number: 7 Primary_atype: Research Publisher: Nature Publishing Group Subject_term: Climate-change impacts;Ocean sciences;Physical oceanography Subject_term_id: climate-change-impacts;ocean-sciences;physical-oceanography.

Cheng, D., Hayes, W., and Larour, E. (2020). Calfin: Calving front dataset for east/west greenland, 1972-2019.

Cheng, D., Hayes, W., Larour, E., Mohajerani, Y., Wood, M., Velicogna, I., and Rignot, E. (2021). Calving front machine (CALFIN): Glacial termini dataset and automated deep learning extraction method for Greenland, 1972-2019. *Cryosphere*, 15(3):1663–1675.

Chollet, F. (2017). Xception: Deep learning with depthwise separable convolutions. *Computer Vision and Pattern Recognition*, pages 1800–1807.

Cowton, T. R., Sole, A. J., Nienow, P. W., Slater, D. A., and Christoffersen, P. (2018). Linear response of east Greenland's tidewater glaciers to ocean/atmosphere warming. *Proceedings of the National Academy of Sciences*, 115(31):7907 – 7912.

ENVEO (2017). Greenland calving front dataset, 1990 - 2016, v3.0. http://products.esa-icesheets-cci.org/products/downloadlist/CFL/.

Fahrner, D., Lea, J. M., Brough, S., Mair, D. W. F., and Abermann, J. (2021). Linear response of the Greenland ice sheet's tidewater glacier terminus positions to climate. *Journal of Glaciology*, 67(262):193–203.

Fürst, J. J., Goelzer, H., and Huybrechts, P. (2015). Ice-dynamic projections of the greenland ice sheet in response to atmospheric and oceanic warming. *The Cryosphere*, 9(3):1039–1062.

Gilbert, E. and Kittel, C. (2021). Surface melt and runoff on Antarctic ice shelves at 1.5°C, 2°C and 4°C of future warming. *Geophysical Research Letters*.

Goliber, S., Black, T., Catania, G., Lea, J. M., Olsen, H., Cheng, D., Bevan, S., Bjørk, A., Bunce, C., Brough, S., Carr, J. R., Cowton, T., Gardner, A., Fahrner, D., Hill, E., Joughin, I., Korsgaard, N., Luckman, A., Moon, T., Murray, T., Sole, A., Wood, M., and Zhang, E. (2021). Termpicks: A century of greenland glacier terminus data for use in machine learning applications. *The Cryosphere Discussions*, 2021:1–41.

Group, W. G. S. L. B. (2018). Global sea-level budget 1993–present. *Earth System Science Data*, 10(3):1551–1590.

Hill, E., Carr, J. R., and Stokes, C. R. (2017). A Review of Recent Changes in Major Marine-Terminating Outlet Glaciers in Northern Greenland. *Frontiers in Earth Science*, 4:111.

Hill, E. A., Carr, J. R., Stokes, C. R., and Gudmundsson, G. H. (2018). Dynamic changes in outlet glaciers in northern Greenland from 1948 to 2015. *The Cryosphere*, pages 1 – 39.

Joughin, I., Moon, T., Joughin, J., and Black, T. (2015). Measures annual greenland outlet glacier terminus positions from sar mosaics, version 1.

Khazendar, A., Rignot, E., and Larour, E. (2007). Larsen B Ice Shelf rheology preceding its disintegration inferred by a control method. *Geophysical Research Letters*, 34(19):19503.

King, M. D., Howat, I. M., Candela, S. G., Noh, M. J., Jeong, S., Noël, B. P. Y., Broeke, M. R. v. d., Wouters, B., and Negrete, A. (2020). Dynamic ice loss from the greenland ice sheet driven by sustained glacier retreat. *Nature News*, 1(1).

Korsgaard, N. (2021). Greenland Ice Sheet outlet glacier terminus positions 1978-1987 from aero-photogrammetric map data. Technical report.

Kruskal, J. B. (1956). On the shortest spanning subtree of a graph and the traveling salesman problem. *Proceedings of the American Mathematical Society*, 7(1):48–50.

Lai, C. Y. et al. (2020). Vulnerability of Antarctica's ice shelves to meltwater-driven fracture. *Nature*, 584(7822):574–578.

Larour, E., Rignot, E., Poinelli, M., and Scheuchl, B. (2021). Physical processes controlling the rifting of Larsen C Ice Shelf, Antarctica, prior to the calving of iceberg A68 in 2017. In review.

Larour, E., Seroussi, H., Morlighem, M., and Rignot, E. (2012). Continental scale, high order, high spatial resolution, ice sheet modeling using the Ice Sheet System Model (ISSM). *Journal of Geophysical Research: Earth Surface*, 117(1):1022.

Mannor, S., Peleg, D., and Rubinstein, R. (2005). The cross entropy method for classification. In *Proceedings of the 22nd International Conference on Machine Learning*, ICML '05, page 561–568, New York, NY, USA. Association for Computing Machinery.

Marsh, O. J., Price, D., Courville, Z. R., and Floricioiu, D. (2021). Crevasse and rift detection in Antarctica from TerraSAR-X satellite imagery. *Cold Regions Science and Technology*, 187.

Mohajerani, Y., Wood, M., Velicogna, I., and Rignot, E. (2019). Detection of glacier calving margins with convolutional neural networks: A case study. *Remote Sensing*, 11(1).

Moon, T. and Joughin, I. (2008). Changes in ice front position on greenland's outlet glaciers from 1992 to 2007. *Journal of Geophysical Research: Earth Surface*, 113(F2).

Morlighem, M., Williams, C. N., Rignot, E., An, L., Arndt, J. E., Bamber, J. L., Catania, G., Chauché, N., Dowdeswell, J. A., Dorschel, B., Fenty, I., Hogan, K., Howat, I., Hubbard, A., Jakobsson, M., Jordan, T. M., Kjeldsen, K. K., Millan, R., Mayer, L., Mouginot, J., Noël, B. P. Y., O'Cofaigh, C., Palmer, S., Rysgaard, S., Seroussi, H., Siegert, M. J., Slabon, P., Straneo, F., van den Broeke, M. R., Weinrebe, W., Wood, M., and Zinglersen, K. B. (2017). Bedmachine v3: Complete bed topography and ocean bathymetry mapping of greenland from multibeam echo sounding combined with mass conservation. *Geophysical Research Letters*, 44(21):11,051–11,061.

Murray, T., Scharrer, K., Selmes, N., Booth, A. D., James, T. D., Bevan, S. L., Bradley, J. A., Cook, S., Llana, L. C., Drocourt, Y., Dyke, L. M., Goldsack, A., Hughes, A. L. C., Luckman, A. J., and McGovern, J. (2015). Extensive Retreat of Greenland Tidewater Glaciers, 2000–2010. *Arctic, Antarctic, and Alpine Research*, 47(3):427 – 447.

Nagler, T., Rott, H., Hetzenecker, M., Wuite, J., and Potin, P. (2015). The sentinel-1 mission: New opportunities for ice sheet observations. *Remote Sensing*, 7(7):9371–9389.

Nick, F. M., Vieli, A., Andersen, M. L., Joughin, I., Payne, A., Edwards, T. L., Pattyn, F., and van de Wal, R. S. W. (2013). Future sea-level rise from greenland's main outlet glaciers in a warming climate. *Nature*, 497(7448):235–238.

Paravolidakis, V., Moirogiorgou, K., Ragia, L., Zervakis, M., and Synolakis, C. (2016). Coastline extraction from aerial images based on edge detection. *ISPRS Annals of Photogrammetry, Remote Sensing and Spatial Information Sciences*, III-8:153–158.

Raup, B., Racoviteanu, A., Khalsa, S. J. S., Helm, C., Armstrong, R., and Arnaud, Y. (2007). The GLIMS geospatial glacier database: A new tool for studying glacier change. *Global and Planetary Change*, 56(1-2):101–110.

Rebesco, M., Domack, E., Zgur, F., Lavoie, C., Leventer, A., Brachfeld, S., Willmott, V., Halverson, G., Truffer, M., Scambos, T., Smith, J., and Pettit, E. (2014). Boundary condition of grounding lines prior to collapse, Larsen-B Ice Shelf, Antarctica. *Science*, 345(6202):1354–1358.

Ronneberger, O., Fischer, P., and Brox, T. (2015). U-net: Convolutional networks for biomedical image segmentation. *CoRR*, abs/1505.04597.

Scambos, T. A., Bohlander, J. A., Shuman, C. A., and Skvarca, P. (2004). Glacier acceleration and thinning after ice shelf collapse in the Larsen B embayment, Antarctica. *Geophysical Research Letters*, 31(18):18402.

Seale, A., Christoffersen, P., Mugford, R. I., and O'Leary, M. (2011). Ocean forcing of the greenland ice sheet: Calving fronts and patterns of retreat identified by automatic satellite monitoring of eastern outlet glaciers. *Journal of Geophysical Research: Earth Surface*, 116(F3).

Stokes, C. R., Sanderson, J. E., Miles, B. W. J., Jamieson, S. S. R., and Leeson, A. A. (2019). Widespread distribution of supraglacial lakes around the margin of the east antarctic ice sheet. *Scientific Reports*, 9(1):13823.

van den Broeke, M. R., Enderlin, E. M., Howat, I. M., Kuipers Munneke, P., Noël, B. P. Y., van de Berg, W. J., van Meijgaard, E., and Wouters, B. (2016). On the recent contribution of the greenland ice sheet to sea level change. *The Cryosphere*, 10(5):1933–1946.

Vansteenwegen, P. and Oudheusden, D. V. (2007). The mobile tourist guide: An or opportunity. *OR Insight*, 20(3):21–27.

Wood, M., Rignot, E., Fenty, I., An, L., Bjørk, A., van den Broeke, M., Cai, C., Kane, E., Menemenlis, D., Millan, R., Morlighem, M., Mouginot, J., Noël, B., Scheuchl, B., Velicogna, I., Willis, J. K., and Zhang, H. (2021). Ocean forcing drives glacier retreat in greenland. *Science Advances*, 7(1).

Zhang, E., Liu, L., and Huang, L. (2019). Automatically delineating the calving front of jakobshavn isbræ from multi-temporal terrasar-x images: a deep learning approach. *The Cryosphere*, 2019:1–20.

Appendix A

Supplementary Material

A.1 Temporal Availability

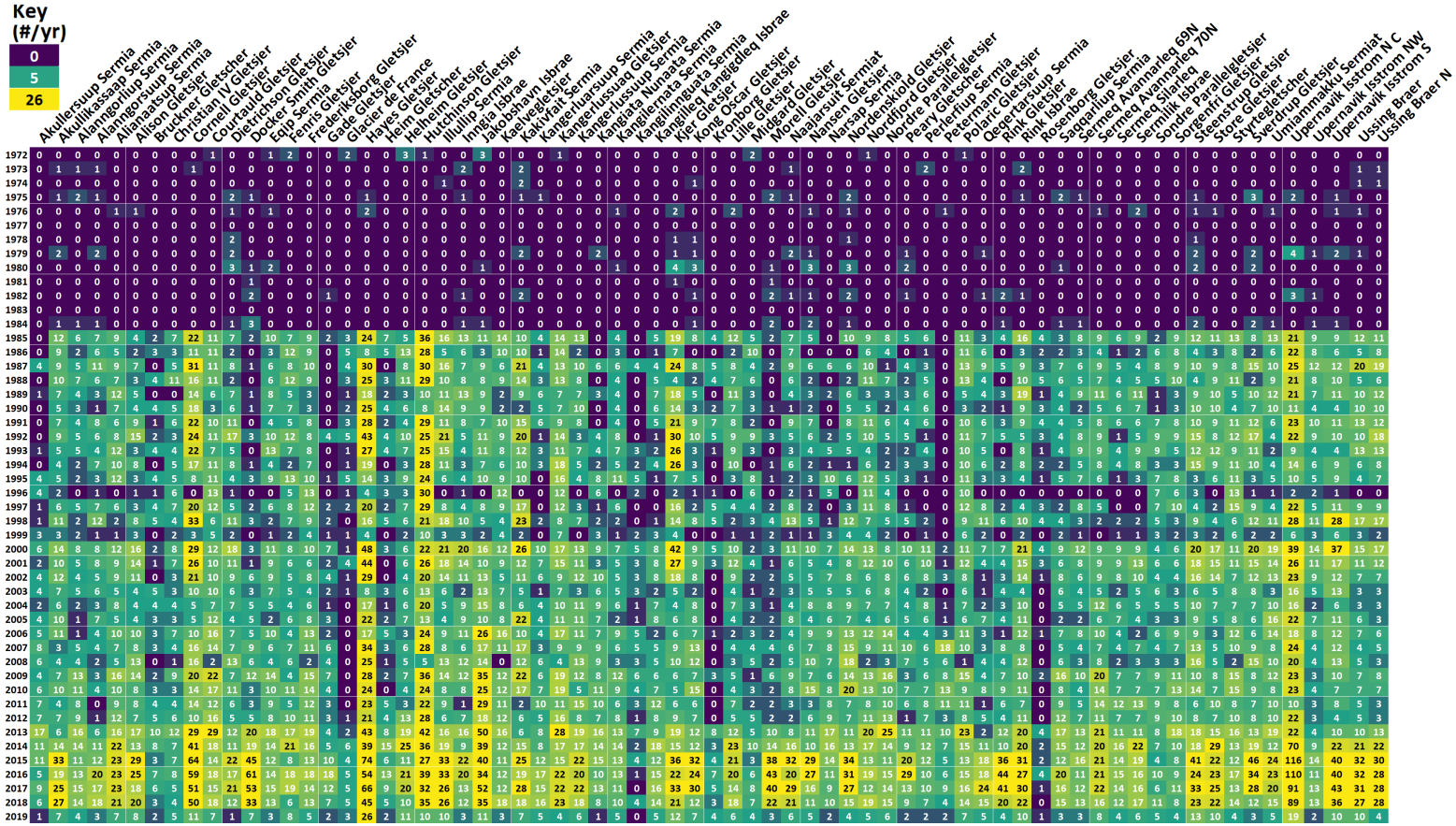

Figure A1: **Temporal Availability Chart**. Listed are the number of fronts per year, for all 66 glaciers in the CALFIN dataset.

A.2 Inter-model Comparison Table

Table A1: **Consolidated validation set and inter-model error metrics.**

Validation Set	Model	Mean Distance	Median Distance	IoU Coastline	IoU Ice/Ocean
CALFIN-VS	CALFIN-NN	2.25 px, 86.76 m	1.21 px, 44.59 m	0.4884	0.9793
CALFIN-VS-L7-none	CALFIN-NN	2.27 px, 81.65 m	1.16 px, 44.01 m	0.4880	0.9819
CALFIN-VS-L7-only	CALFIN-NN	2.22 px, 91.93 m	1.33 px, 49.24 m	0.4888	0.9766
M-VS	CALFIN-NN	2.56 px, 97.72 m	2.55 px, 97.44 m	0.3332	N/A
M-VS	M-NN	1.97 px, 96.31 m	N/A	N/A	N/A
Z-VS	CALFIN-NN	2.11 px, 115.24 m	1.65 px, 77.29 m	0.3832	0.9761
Z-VS	Z-NN	17.3 px, 104 m	N/A	N/A	N/A
B-VS	CALFIN-NN	2.35 px, 330.63 m	0.74 px, 112.75 m	0.6451	0.9879
B-VS	B-NN	2.69 px, 108 m	N/A	N/A	0.905

A.3 Dataset Metadata

Level 0 products consist of fjord boundary GeoTiff masks, the domain Shapefiles used for subsetting, and the Landsat scene name list text files. Level 1 product consists of a LineString Shapefile with 22678 features, and a Polygon Shapefile with 17771 features, grouped by glacial basin. Both Shapefiles share a feature schema derived from the MEaSUREs glacial terminus positions dataset (NSIDC-0642), as detailed in Table A2.

- Temporal resolution: sub-seasonal
- Spatial resolution: ˜30 meters

- Spatial accuracy: <90 meters
- Projection: EPSG:3413 (WGS 84 / NSIDC Sea Ice Polar Stereographic North)

Table A2: **Shapefile Feature Schema Attribute Table**

Data Field	Description	Format (Values)
GlacierID	Numerical ID assigned to each glacier (as derived from MEaSUREs NSIDC-0642)	# ([1, 246])
Center_X	Mean X coordinate in EPSG:3413.	# ([-463626, 682313])
Center_Y	Mean Y coordinate in EPSG:3413.	# ([-2821269, -906747])
Latitude	Latitude of center.	# ([64.29, 81.24])
Longitude	Longitude of center.	# ([-63.17, -28.21])
QualFlag	Quality flag to indicate digitization conditions	# (0 – Manually digitized, 3 – Manually digitized, w/ L7 SCE, 10 - Automatically digitized, 13 – Automatically digitized, w/ L7 SCE. See MEaSUREs NSIDC-0642)
Sattellite	Satellite/sensor of the digitized source image	LXSS ([LM01, LC08]) See https://www.usgs.gov/faqs/what-naming-convention-landsat-collections-level-1-scenes
Date	Date of the digitized source image	YYYY-MM-DD ([1972-09-06, 2019-06-25])
ImageID	Source image file name.	LXSS_LLLL_PPPRRR_YYYYMMDD_yyyymmdd_CC_TX (LC08_L1TP_026006_20170702_20170715_01_T1, etc.)
GrnlndcN	Greenlandic glacier name	NAME (New_Greenl names from Bjørk et al., 2015 database of Greenland glacier names)
OfficialN	Officially recognized glacier name	NAME (Official_n names from Bjørk et al., 2015 database of Greenland glacier names)
AltName	Alternative, Foreign, Old Greenlandic, or other glacier names	NAME (Foreign_na, Old_Greenl, Alternative names (Bjørk et al., 2015), or other names)
RefName	Reference glacier name, non-authoritative names used in CALFIN to denote grouped/unnamed glaciers	NAME (New_Greenl, Official_n, Foreign_na, Old_Greenl, Alternative names (Bjørk et al., 2015), or other names)
Author	Digitization author's name	LastName_FirstInitial (Cheng_D)

A.4 Error Estimation

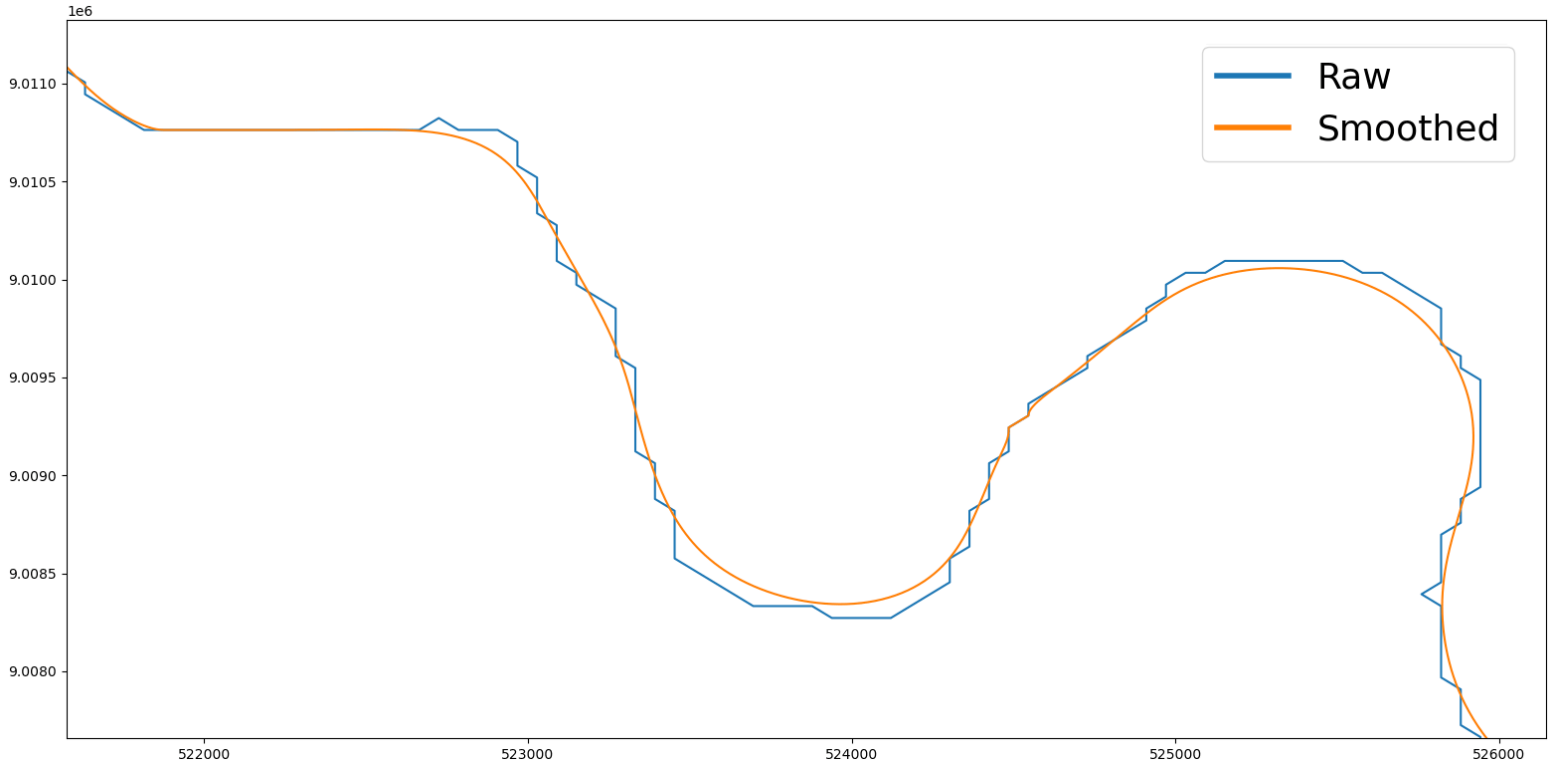

Figure A2: **Smoothed versus Raw Polyline** The post-processing line smoothing operation turns the raw coastline (blue) into a smoothed data product polyline (orange), deviating by no more than 1 pixel from the raw coastline. Since the variations are on the sub-pixel scale, the error introduced is no more than the uncertainty of the base resolution, and well within the neural network uncertainty.

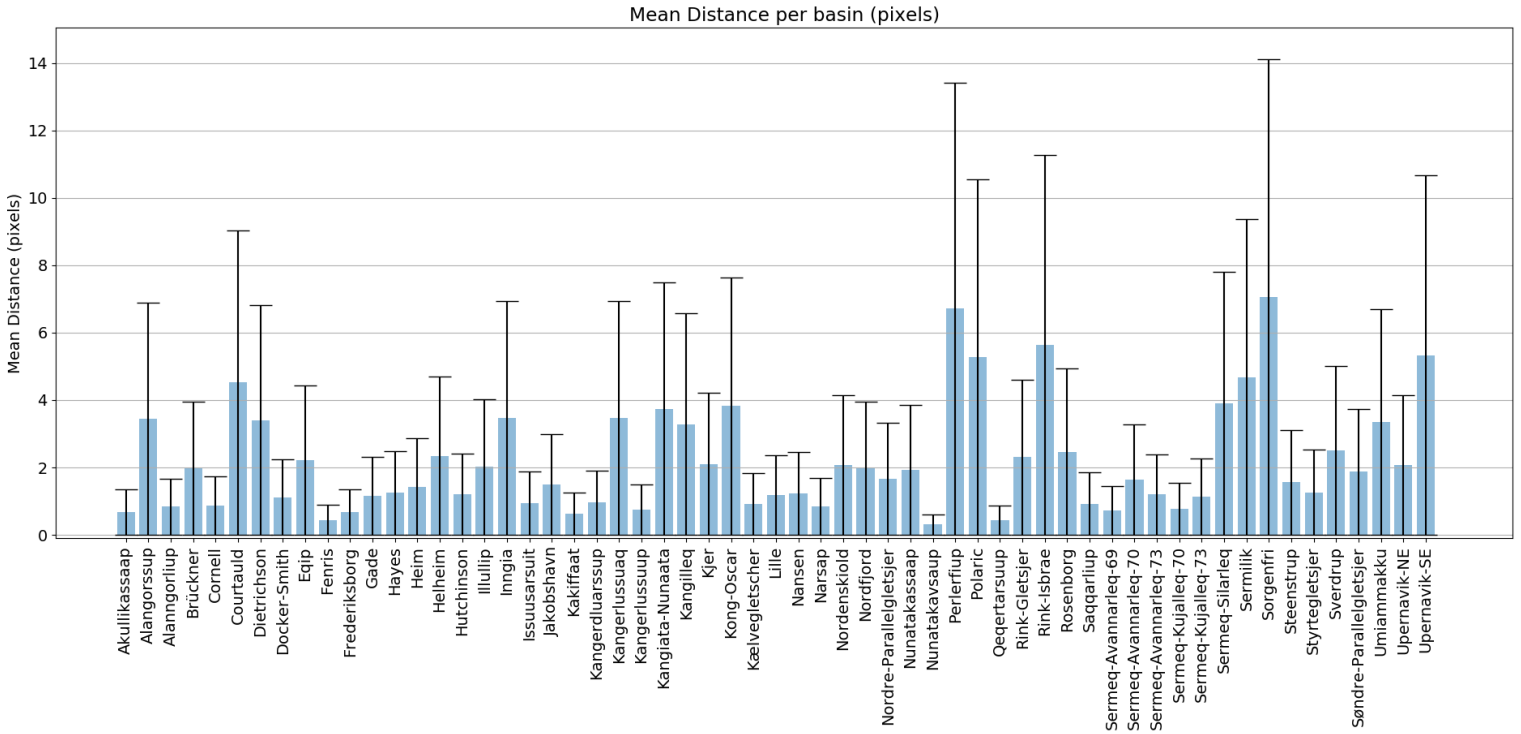

Figure A3: **True mean distance error estimates per basin, in pixels.** We estimate the true mean distance error per basin to lie between the above intervals with 95% confidence.

A.5 Training Data

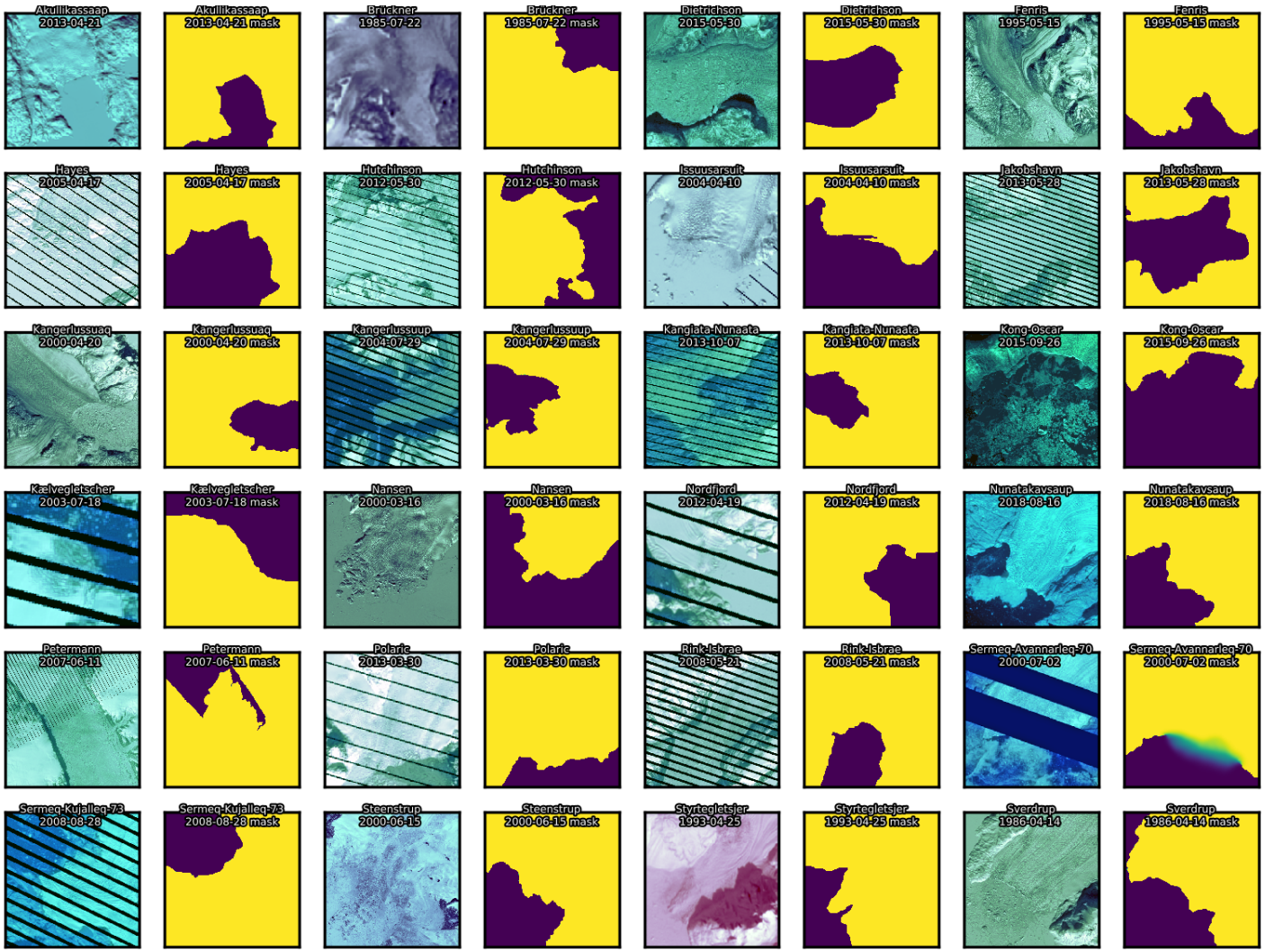

Figure A4: **CALFIN-NN training data**. Shown above is a subset of the 1872 CALFIN-NN training image/mask pairs. Not shown are the coastline masks, which are dynamically generated after performing data augmentation on the above masks, using Canny edge filters and dilation to a 3 pixel wide edge. Note blurred mask in uncertain areas, as in Sermeq Avannarleq 70 2000-07-02. Images are masked at a minimum resolution of 1024 pixels.

A.6 Validation Data

A.6.1 CALFIN Validation Set

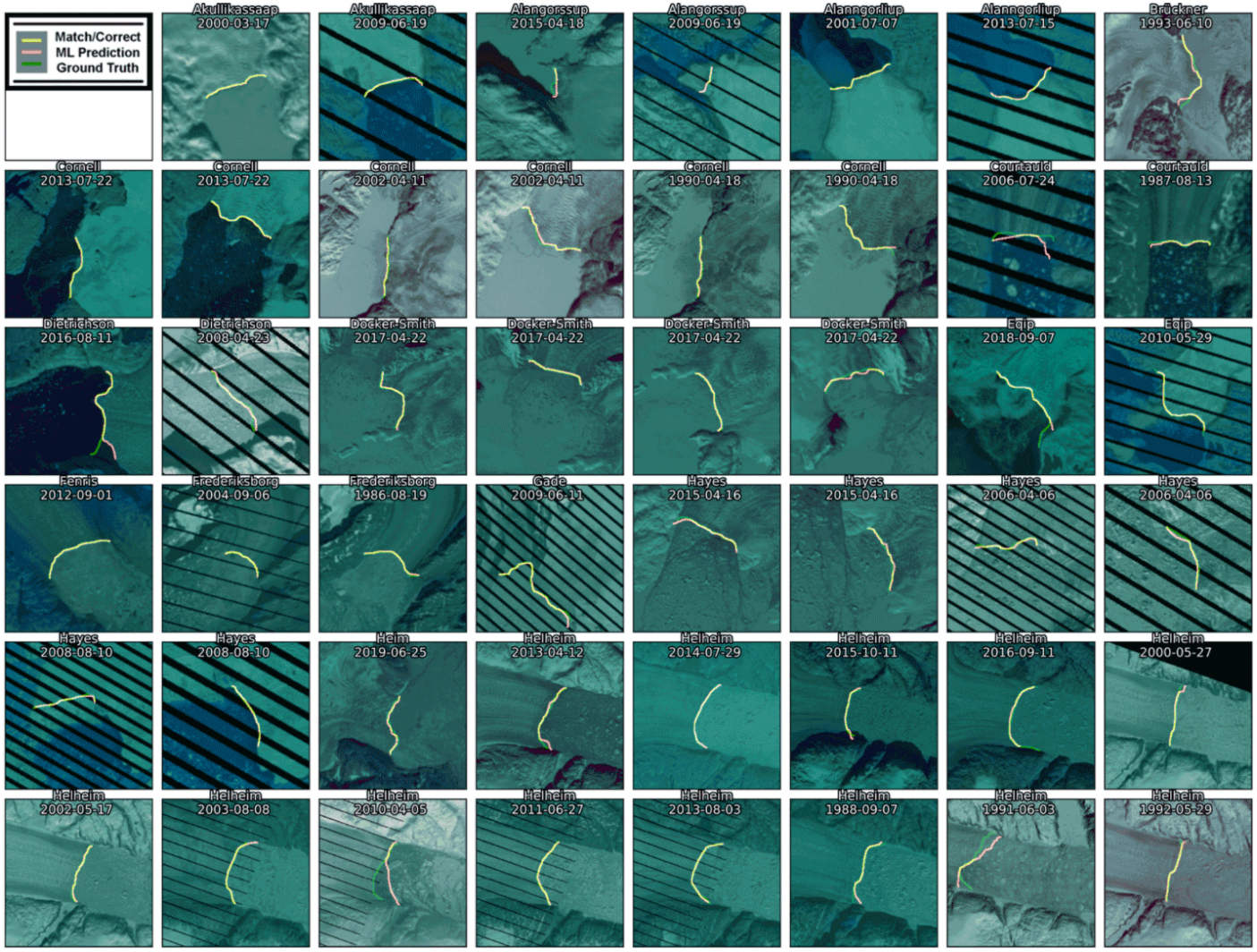

Figure A5: **CALFIN validation outputs, part 1**.

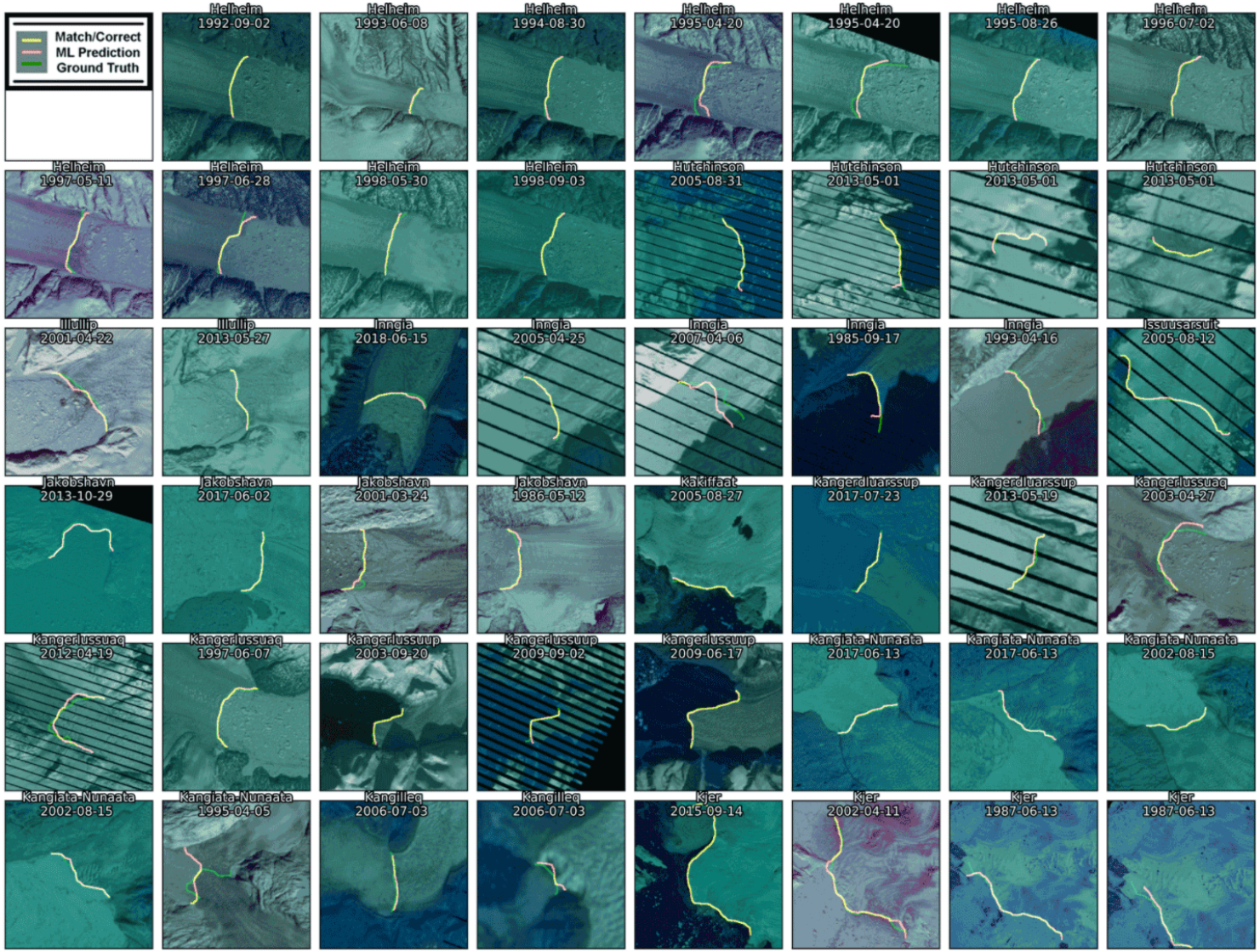

Figure A6: **CALFIN validation outputs, part 2**.

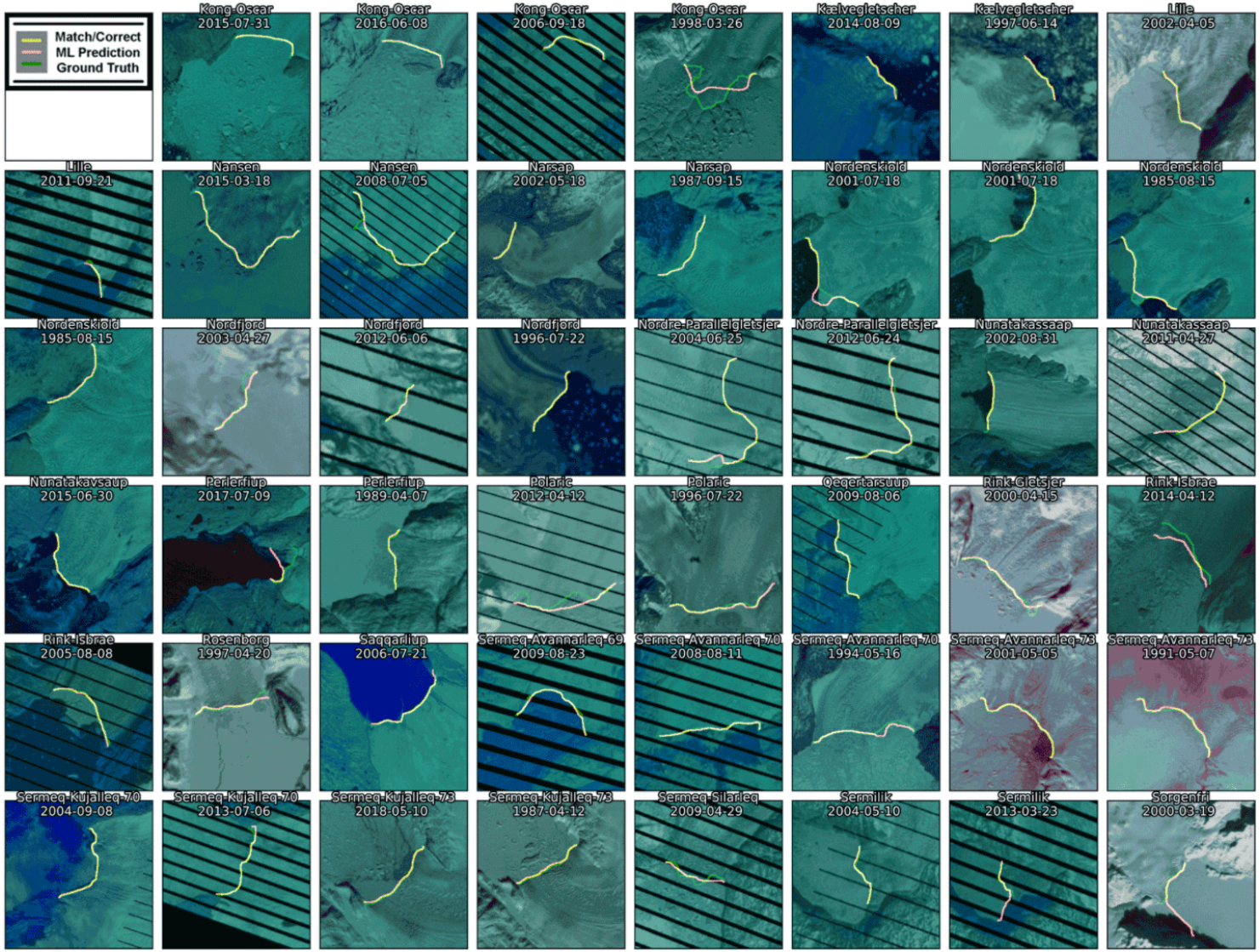

Figure A7: **CALFIN validation outputs, part 3**.

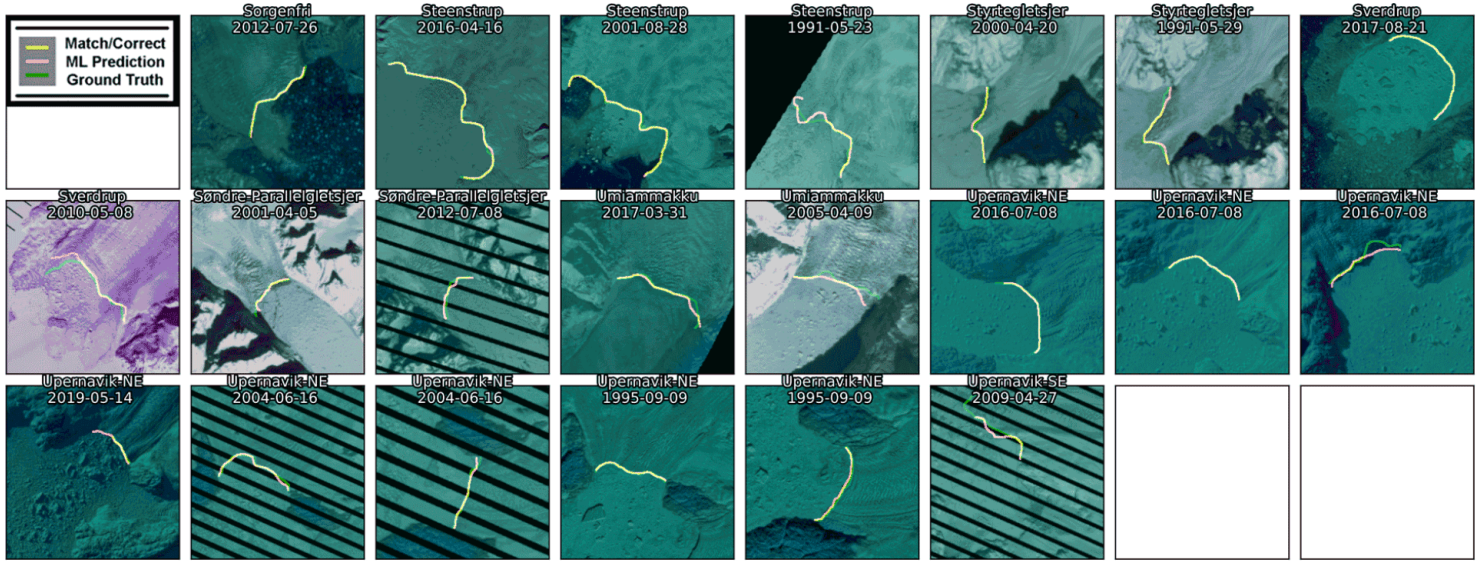

Figure A8: **CALFIN validation outputs, part 4**.

A.6.2 Mohajerani et al. Validation Set

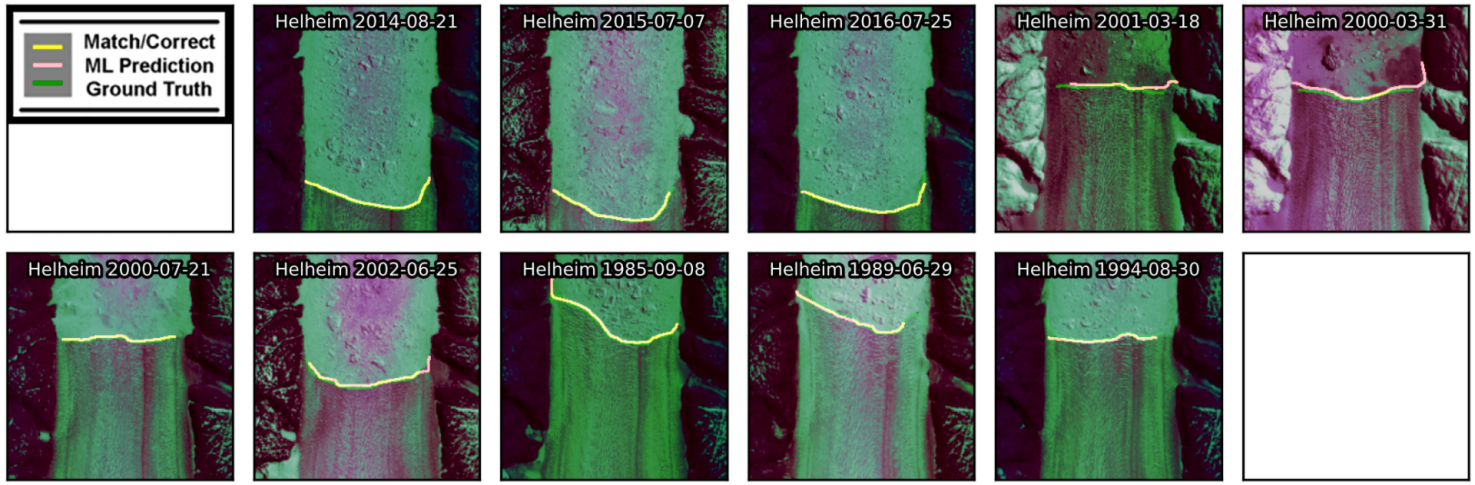

Figure A9: **Mohajerani et al. validation outputs**.

A.6.3 Zhang et al. Validation Set

Figure A10: **Zhang et al. validation outputs**. Note that there are missing subsets where CALFIN did not detect any fronts, despite them being visible.

A.6.4 Baumhoer et al. Validation Set

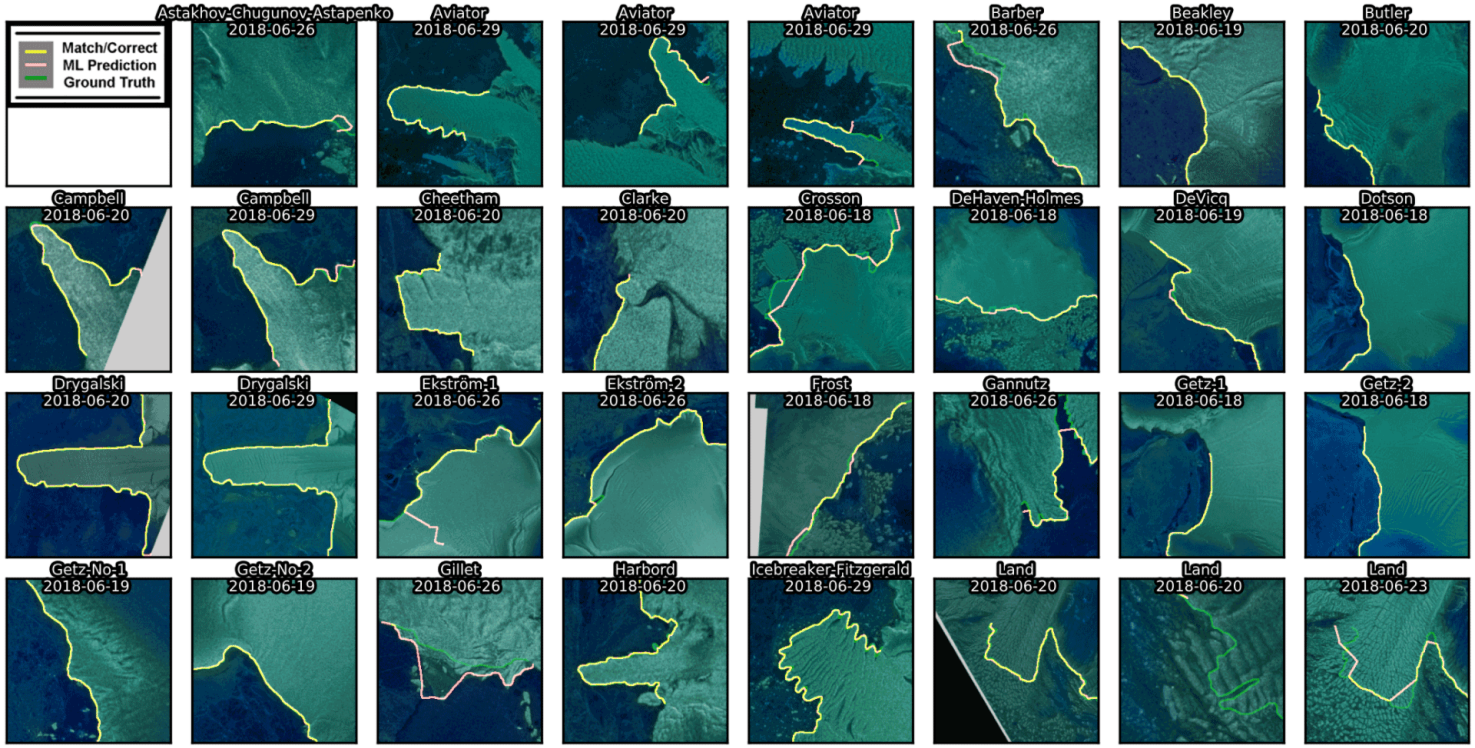

Figure A11: **Baumhoer et al. validation outputs, part 1**. Large errors originate from Ekstrom-1, Gillet, Land, and other similar domains.

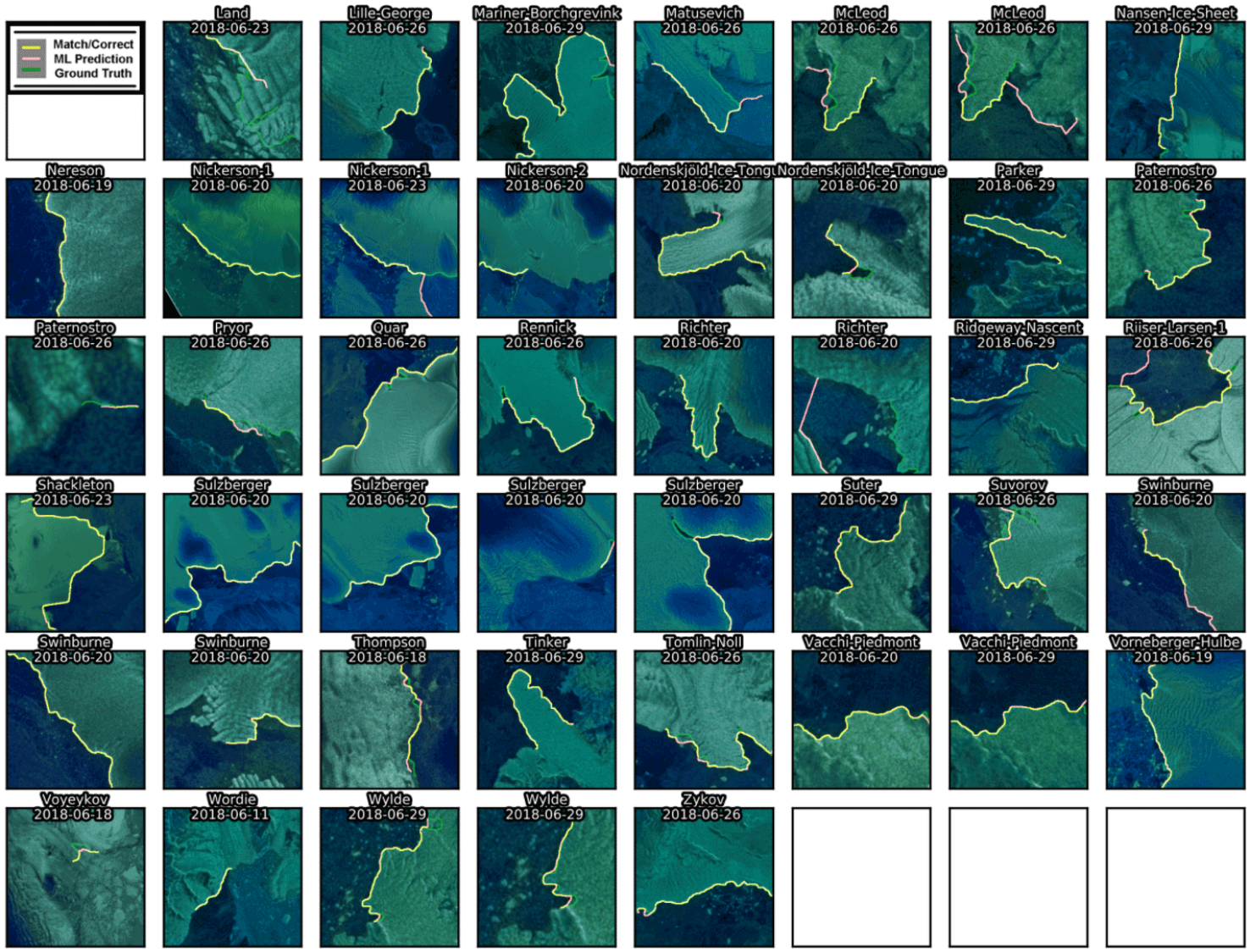

Figure A12: **Baumhoer et al. validation outputs, part 2**. Note that Wordie and Voyeykov, among others, have not been fully nor confidently detected.

A.7 CALFIN Validation Set Scene ID List

Table A3: **CALFIN Validation Set Scene ID List**. A list of all 162 images used in the CALFIN-VS.

Domain	Scene ID	Domain	Scene ID
Akullikassaap	LE07_L1TP_014009_20000317_20170212_01_T1	Akullikassaap	LE07_L1TP_017008_20090619_20161221_01_T1
Alangorssup	LC08_L1TP_016008_20150418_20170409_01_T1	Alangorssup	LE07_L1TP_017008_20090619_20161221_01_T1
Alanngorliup	LE07_L1TP_009011_20010707_20170204_01_T1	Alanngorliup	LE07_L1TP_010011_20130715_20161123_01_T1
Brückner	LT05_L1TP_231014_19930610_20180228_01_T2	Cornell	LC08_L1TP_019007_20130722_20170503_01_T1
Cornell	LE07_L1TP_019007_20020411_20170131_01_T1	Cornell	LT05_L1TP_019007_19900418_20170130_01_T1
Courtauld	LE07_L1TP_231012_20060724_20170109_01_T1	Courtauld	LT05_L1TP_231012_19870813_20170211_01_T1
Dietrichson	LC08_L1TP_023006_20160811_20170322_01_T1	Dietrichson	LE07_L1TP_023006_20080423_20161229_01_T1
Docker-Smith	LC08_L1TP_025006_20170422_20170501_01_T1	Eqip	LC08_L1TP_010011_20180907_20180912_01_T1
Eqip	LE07_L1TP_009011_20100529_20161215_01_T1	Fenris	LE07_L1TP_232013_20120901_20161128_01_T1
Frederiksborg	LE07_L1TP_229012_20040906_20170119_01_T1	Frederiksborg	LT05_L1TP_230012_19860819_20170216_01_T1
Gade	LE07_L1TP_025006_20090611_20161219_01_T1	Hayes	LC08_L1TP_018007_20150416_20170409_01_T1
Hayes	LC08_L1TP_080237_20160607_20170324_01_T1	Hayes	LE07_L1TP_019007_20060406_20170110_01_T1
Hayes	LE07_L1TP_018007_20080810_20161225_01_T1	Heim	LC08_L1TP_232014_20190625_20190625_01_RT
Helheim	LC08_L1TP_233013_20130412_20170505_01_T1	Helheim	LC08_L1TP_232014_20140729_20170420_01_T1
Helheim	LC08_L1TP_233013_20151011_20170403_01_T1	Helheim	LC08_L1TP_233013_20160911_20170321_01_T1
Helheim	LC08_L1TP_232013_20180606_20180615_01_T1	Helheim	LE07_L1TP_232014_20000527_20170211_01_T1

Continued on next page

Table A3 – *Continued from previous page*

Domain	Scene ID	Domain	Scene ID
Helheim	LE07_L1TP_232013_20020517_20170130_01_T1	Helheim	LE07_L1TP_232013_20030808_20170124_01_T1
Helheim	LE07_L1TP_232013_20060512_20170109_01_T2	Helheim	LE07_L1TP_232013_20100405_20161215_01_T2
Helheim	LE07_L1TP_232013_20110627_20161208_01_T1	Helheim	LE07_L1TP_232013_20130803_20161123_01_T1
Helheim	LT05_L1TP_232014_19860817_20170216_01_T1	Helheim	LT05_L1TP_232013_19880907_20170206_01_T1
Helheim	LT05_L1TP_233013_19910603_20180228_01_T2	Helheim	LT05_L1TP_232013_19910714_20180228_01_T1
Helheim	LT05_L1TP_232013_19920529_20180228_01_T2	Helheim	LT05_L1TP_232013_19920614_20180228_01_T2
Helheim	LT05_L1TP_232013_19920902_20180228_01_T1	Helheim	LT05_L1TP_232014_19930430_20180228_01_T2
Helheim	LT05_L1TP_233013_19930608_20180228_01_T2	Helheim	LT05_L1TP_233013_19940830_20170113_01_T2
Helheim	LT05_L1TP_232013_19950420_20180228_01_T2	Helheim	LT05_L1TP_232014_19950420_20180228_01_T2
Helheim	LT05_L1TP_232014_19950826_20180228_01_T1	Helheim	LT05_L1TP_233013_19960702_20180228_01_T1
Helheim	LT05_L1TP_232013_19970511_20180228_01_T2	Helheim	LT05_L1TP_232013_19970628_20180228_01_T1
Helheim	LT05_L1TP_232013_19980530_20161224_01_T1	Helheim	LT05_L1TP_232013_19980903_20161222_01_T1
Hutchinson	LE07_L1TP_230012_20050831_20170114_01_T1	Hutchinson	LE07_L1TP_230012_20130501_20161124_01_T2
Illullip	LE07_L1TP_021007_20010422_20170206_01_T1	Illullip	LE07_L1TP_019007_20130527_20161124_01_T1
Inngia	LC08_L1TP_014009_20180615_20180703_01_T1	Inngia	LE07_L1TP_013009_20050425_20170115_01_T1
Inngia	LE07_L1TP_014009_20070406_20170104_01_T1	Inngia	LT05_L1TP_013009_19850917_20170218_01_T1
Inngia	LT05_L1TP_013009_19930416_20180220_01_T1	Issuusarsuit	LE07_L1TP_024006_20050812_20170113_01_T1
Jakobshavn	LC08_L1TP_008012_20131029_20170429_01_T1	Jakobshavn	LC08_L1TP_008012_20170602_20170615_01_T1

Continued on next page

Table A3 – *Continued from previous page*

Domain	Scene ID	Domain	Scene ID
Jakobshavn	LE07_L1TP_010011_20010324_20170206_01_T1	Jakobshavn	LT05_L1TP_008011_19860512_20170218_01_T1
Jakobshavn	LT05_L1TP_008011_19950505_20180220_01_T1	Kakiffaat	LE07_L1TP_017008_20050827_20170114_01_T1
Kangerdluarssup	LC08_L1TP_013009_20170723_20170809_01_T1	Kangerdluarssup	LE07_L1TP_011010_20130519_20161124_01_T1
Kangerlussuaq	LE07_L1TP_231012_20030427_20170125_01_T2	Kangerlussuaq	LE07_L1TP_231012_20120419_20161202_01_T2
Kangerlussuaq	LT05_L1TP_229012_19970607_20180227_01_T1	Kangerlussuup	LE07_L1TP_012010_20030920_20170124_01_T1
Kangerlussuup	LE07_L1TP_014009_20090902_20161220_01_T1	Kangerlussuup	LT05_L1TP_011010_20090617_20161025_01_T1
Kangiata-Nunaata	LC08_L1TP_005015_20170613_20170628_01_T1	Kangiata-Nunaata	LE07_L1TP_005015_20020815_20170128_01_T1
Kangiata-Nunaata	LT05_L1TP_006015_19950405_20170109_01_T1	Kangilleq	LE07_L1TP_011010_20060703_20170109_01_T1
Kjer	LC08_L1TP_019007_20150914_20170404_01_T1	Kjer	LE07_L1TP_019007_20020411_20170131_01_T1
Kjer	LT05_L1TP_019007_19870613_20170212_01_T1	Kong-Oscar	LC08_L1TP_024006_20150731_20170406_01_T1
Kong-Oscar	LC08_L1TP_023006_20160608_20170324_01_T1	Kong-Oscar	LE07_L1TP_022006_20060918_20170107_01_T1
Kong-Oscar	LT05_L1TP_024006_19980326_20161225_01_T1	Kælvegletscher	LC08_L1TP_229012_20140809_20170420_01_T1
Kælvegletscher	LE07_L1TP_231012_20050603_20170114_01_T2	Kælvegletscher	LE07_L1TP_231012_20120825_20161129_01_T1
Kælvegletscher	LT05_L1TP_230012_19970614_20180227_01_T1	Lille	LE07_L1TP_009011_20020405_20170131_01_T1
Lille	LE07_L1TP_009011_20110921_20161206_01_T1	Midgård	LT05_L1TP_232013_19950927_20180228_01_T1
Nansen	LC08_L1TP_023006_20150318_20170412_01_T1	Nansen	LE07_L1TP_022006_20080705_20161228_01_T1
Narsap	LE07_L1TP_006015_20020518_20170130_01_T1	Narsap	LT05_L1TP_005015_19870915_20170211_01_T1
Nordenskiold	LE07_L1TP_022006_20010718_20170204_01_T1	Nordenskiold	LT05_L1TP_022006_19850815_20170219_01_T1

Continued on next page

Table A3 – *Continued from previous page*

Domain	Scene ID	Domain	Scene ID
Nordfjord	LE07_L1TP_231012_20030427_20170125_01_T2	Nordfjord	LE07_L1TP_231012_20120606_20161202_01_T1
Nordfjord	LT05_L1TP_229012_19960722_20180227_01_T1	Nordre-Parallelgletsjer	LE07_L1TP_230012_20040625_20170120_01_T1
Nordre-Parallelgletsjer	LE07_L1TP_229012_20120624_20161130_01_T1	Nordre-Parallelgletsjer	LT05_L1TP_229012_19970522_20180227_01_T2
Nunatakassaap	LE07_L1TP_021007_20020831_20170128_01_T1	Nunatakassaap	LE07_L1TP_020007_20110427_20161209_01_T1
Nunatakavsaup	LC08_L1TP_015008_20150630_20170407_01_T1	Nunatakavsaup	LE07_L1TP_016008_20070522_20170103_01_T1
Perlerfiup	LC08_L1TP_011010_20170709_20170717_01_T1	Perlerfiup	LT05_L1TP_011010_19890407_20170204_01_T1
Polaric	LE07_L1TP_230012_20120412_20161202_01_T2	Polaric	LT05_L1TP_229012_19960722_20180227_01_T1
Qeqertarsuup	LE07_L1TP_017008_20090806_20161218_01_T1	Rink-Gletsjer	LE07_L1TP_025006_20000415_20170212_01_T1
Rink-Isbrae	LC08_L1TP_011010_20140412_20170423_01_T1	Rink-Isbrae	LE07_L1TP_012010_20050808_20170114_01_T1
Rink-Isbrae	LT05_L1TP_013009_19860616_20170217_01_T1	Rink-Isbrae	LT05_L1TP_012010_19900519_20170130_01_T1
Rosenborg	LT05_L1TP_229012_19970420_20180227_01_T2	Saqqarliup	LE07_L1TP_009011_20060721_20170109_01_T1
Sermeq-Avannarleq-69	LC08_L1TP_008012_20181011_20181030_01_T1	Sermeq-Avannarleq-69	LE07_L1TP_008011_20090823_20161218_01_T1
Sermeq-Avannarleq-70	LC08_L1TP_011010_20140428_20170423_01_T1	Sermeq-Avannarleq-70	LE07_L1TP_009011_20080811_20161225_01_T1
Sermeq-Avannarleq-70	LT05_L1TP_010011_19940516_20170115_01_T1	Sermeq-Avannarleq-73	LE07_L1TP_016008_20010505_20170205_01_T1
Sermeq-Avannarleq-73	LT05_L1TP_019007_19910507_20180221_01_T2	Sermeq-Kujalleq-70	LE07_L1TP_010011_20040908_20170119_01_T1
Sermeq-Kujalleq-70	LE07_L1TP_011010_20130706_20161123_01_T1	Sermeq-Kujalleq-73	LC08_L1TP_018008_20180510_20180517_01_T1
Sermeq-Kujalleq-73	LT05_L1TP_017008_19870412_20170213_01_T1	Sermeq-Silarleq	LE07_L1TP_012010_20090429_20161220_01_T1
Sermilik	LE07_L1TP_011010_20040510_20170120_01_T1	Sermilik	LE07_L1TP_012010_20130323_20161124_01_T1

Continued on next page

Table A3 – *Continued from previous page*

Domain	Scene ID	Domain	Scene ID
Sorgenfri	LE07_L1TP_229012_20000319_20170212_01_T2	Sorgenfri	LE07_L1TP_229012_20120726_20161130_01_T1
Steenstrup	LC08_L1TP_020007_20160416_20170326_01_T1	Steenstrup	LE07_L1TP_021007_20010828_20170203_01_T1
Steenstrup	LT05_L1TP_019007_19910523_20180221_01_T1	Styrtegletsjer	LE07_L1TP_229012_20000420_20170212_01_T2
Styrtegletsjer	LE07_L1TP_229012_20100416_20161214_01_T1	Styrtegletsjer	LT05_L1TP_230012_19910529_20180227_01_T1
Sverdrup	LC08_L1TP_024006_20170821_20170911_01_T1	Sverdrup	LE07_L1TP_022006_20100508_20161214_01_T1
Søndre-Parallelgletsjer	LE07_L1TP_231012_20010405_20170205_01_T2	Søndre-Parallelgletsjer	LE07_L1TP_231012_20120708_20161130_01_T1
Umiammakku	LC08_L1TP_015009_20170331_20170414_01_T1	Umiammakku	LE07_L1TP_013009_20050409_20170115_01_T1
Umiammakku	LE07_L1TP_014009_20110620_20161209_01_T1	Upernavik-NE	LC08_L1TP_015008_20130928_20170502_01_T1
Upernavik-NE	LC08_L1TP_082235_20160708_20170323_01_T1	Upernavik-NE	LC08_L1TP_082236_20190514_20190521_01_T1
Upernavik-NE	LE07_L1TP_014009_20040616_20170120_01_T1	Upernavik-NE	LT05_L1TP_017008_19950909_20180220_01_T1
Upernavik-SE	LC08_L1TP_016008_20160506_20170326_01_T1	Upernavik-SE	LE07_L1TP_014009_20090427_20161222_01_T1

A.8 Selected Relative Advance and Retreat Graphs

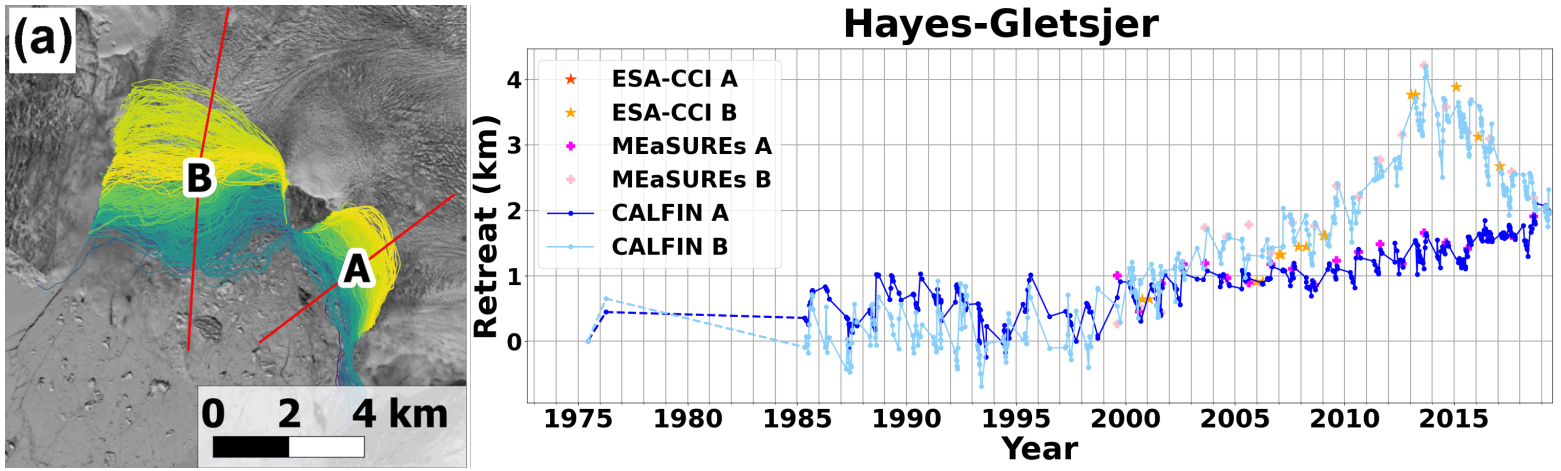

Figure A13: **Terminus Advance and Retreat Over Time for Hayes Gletsjer**. Dotted lines from 1972-1985 that indicate a lack of seasonal observations.

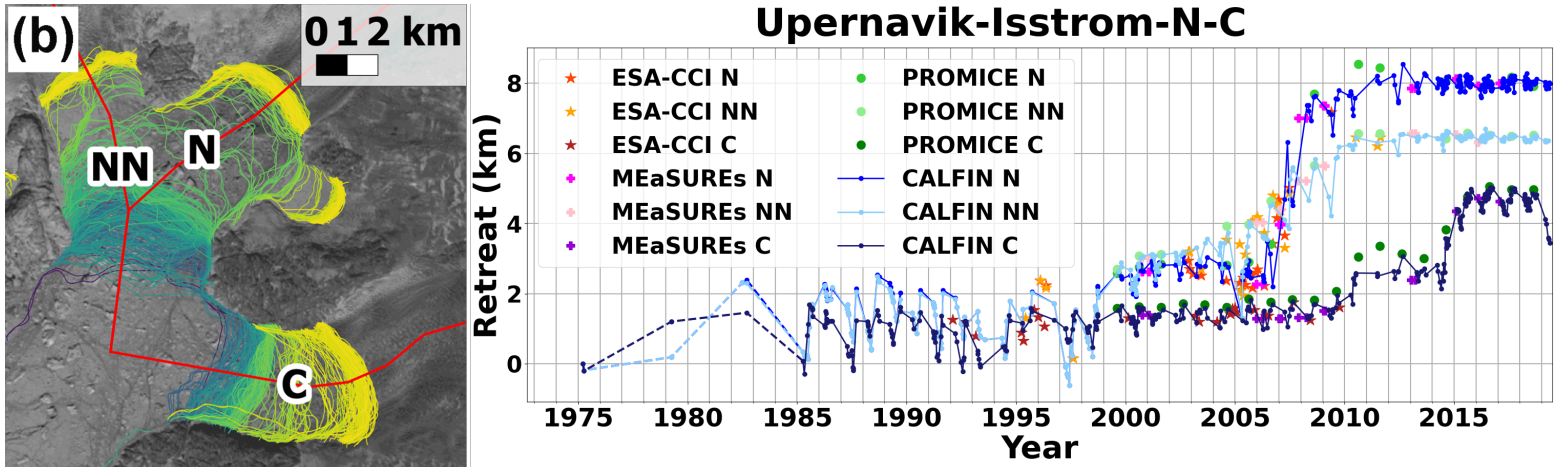

Figure A14: **Terminus Advance and Retreat Over Time for Upernavik Isstrom N-C**. Dotted lines from 1972-1985 that indicate a lack of seasonal observations.

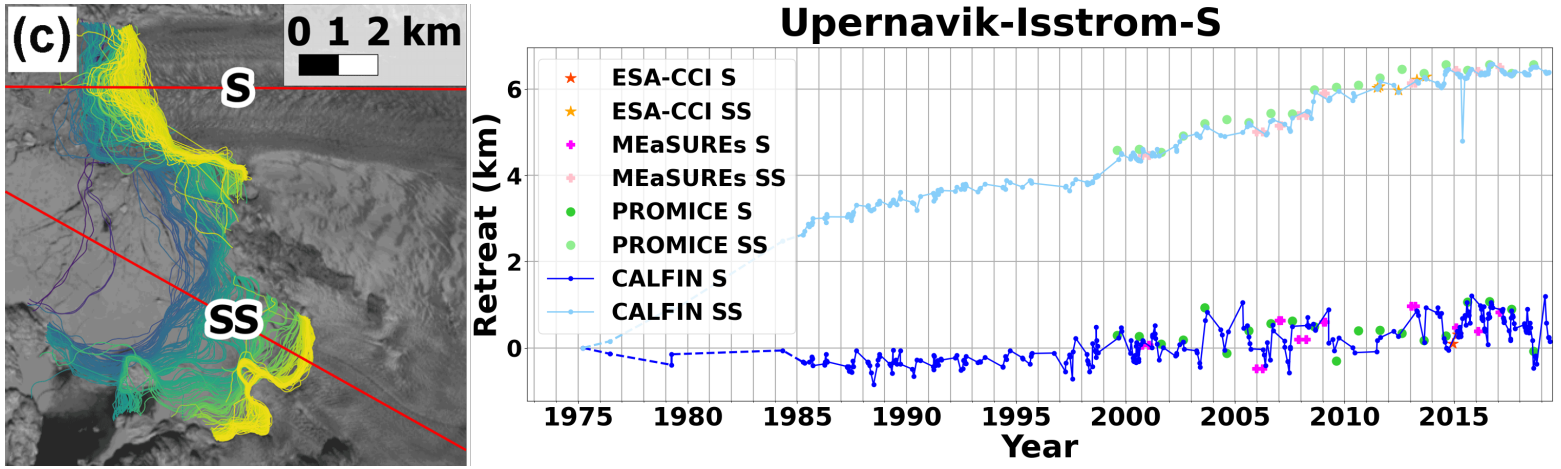

Figure A15: **Terminus Advance and Retreat Over Time for Upernavik Isstrom S**. Dotted lines from 1972-1985 that indicate a lack of seasonal observations.

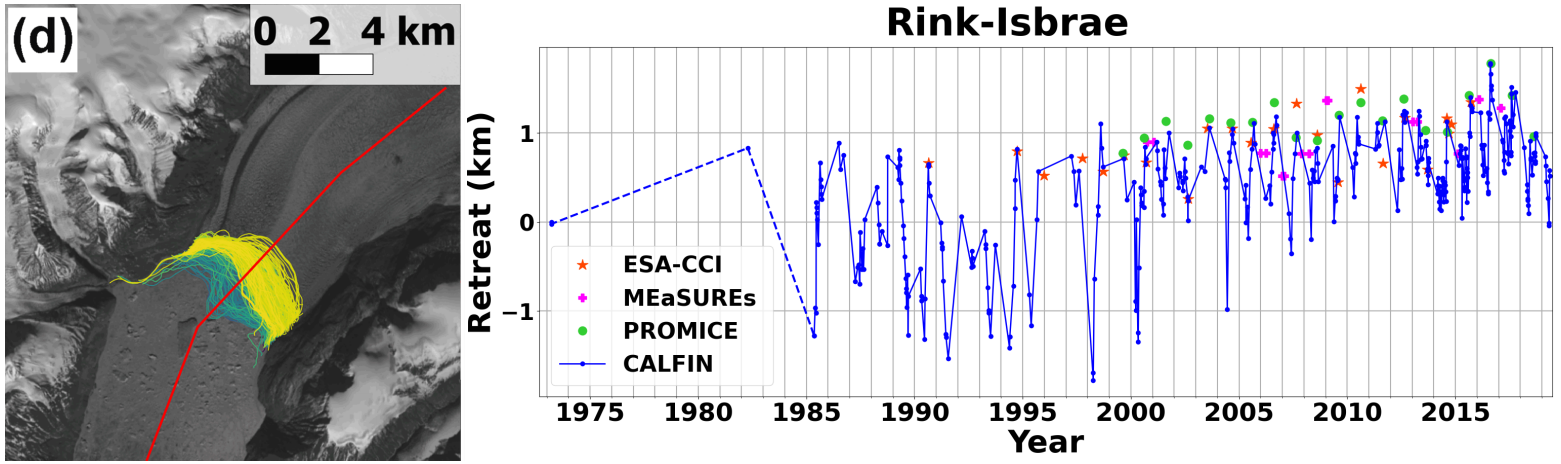

Figure A16: **Terminus Advance and Retreat Over Time for Rink Isbrae**. Dotted lines from 1972-1985 that indicate a lack of seasonal observations.

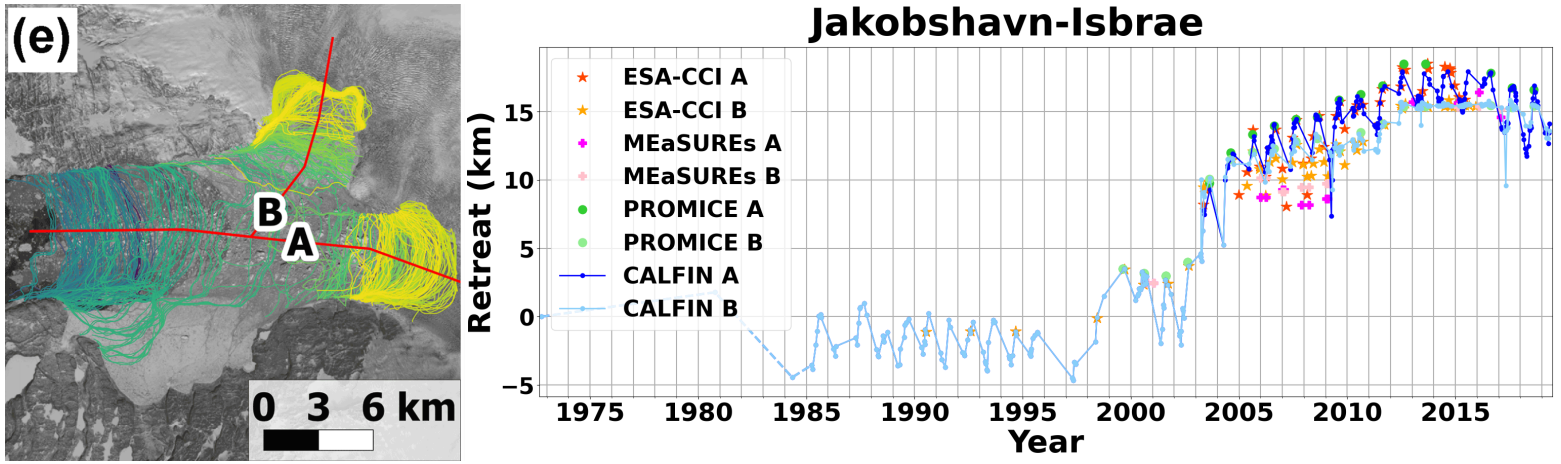

Figure A17: **Terminus Advance and Retreat Over Time for Jakobshavn Isbrae**. Dotted lines from 1972-1985 that indicate a lack of seasonal observations.

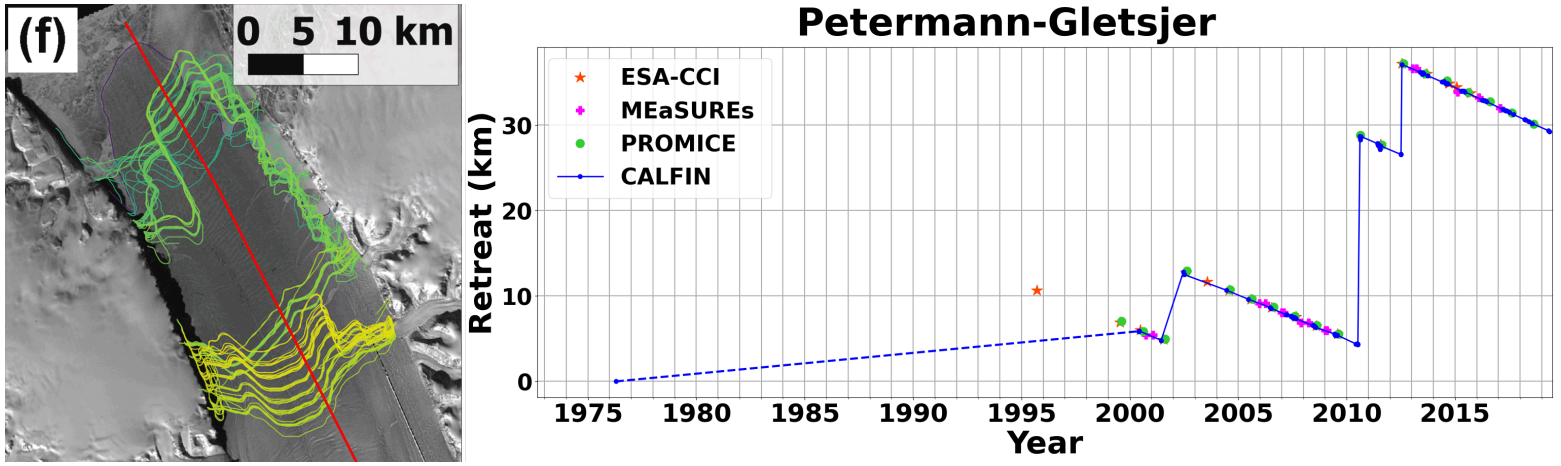

Figure A18: **Terminus Advance and Retreat Over Time for Petermann Gletsjer**. Dotted lines from 1972-1985 that indicate a lack of seasonal observations.

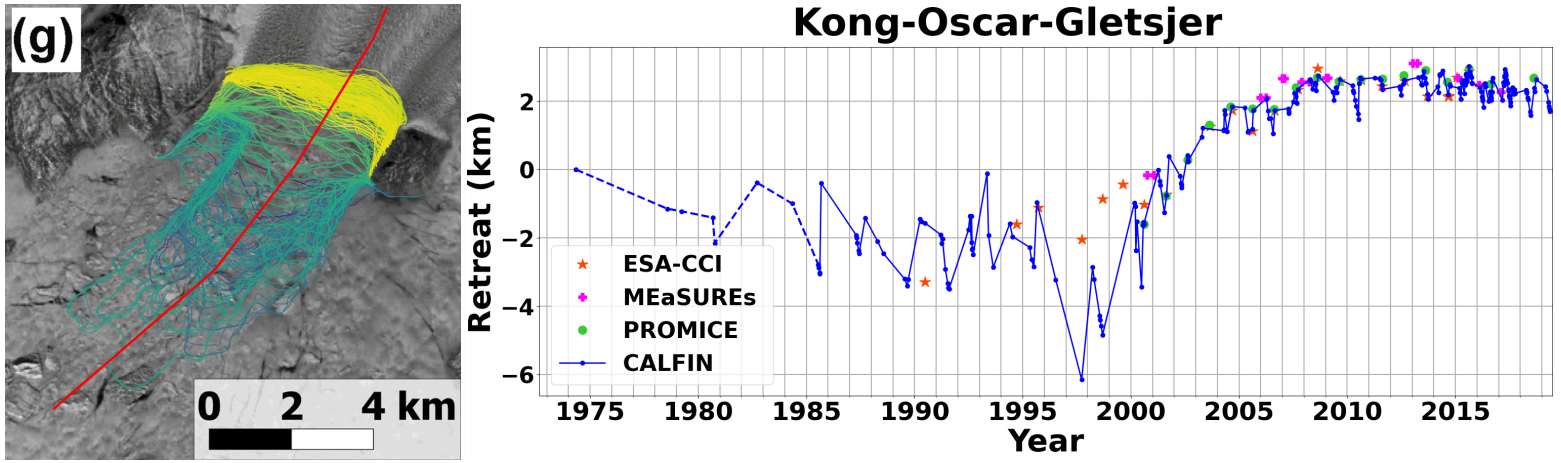

Figure A19: **Terminus Advance and Retreat Over Time for Kong Oscar Gletsjer**. Dotted lines from 1972-1985 that indicate a lack of seasonal observations.

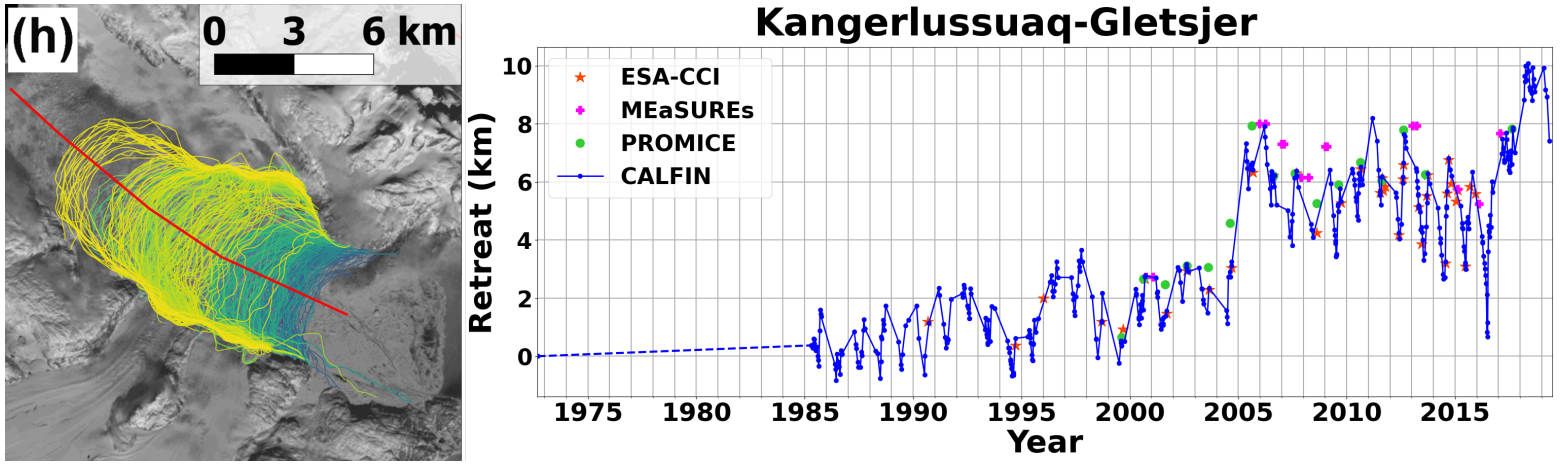

Figure A20: **Terminus Advance and Retreat Over Time for Kangerlussuaq Gletsjer**. Dotted lines from 1972-1985 that indicate a lack of seasonal observations.

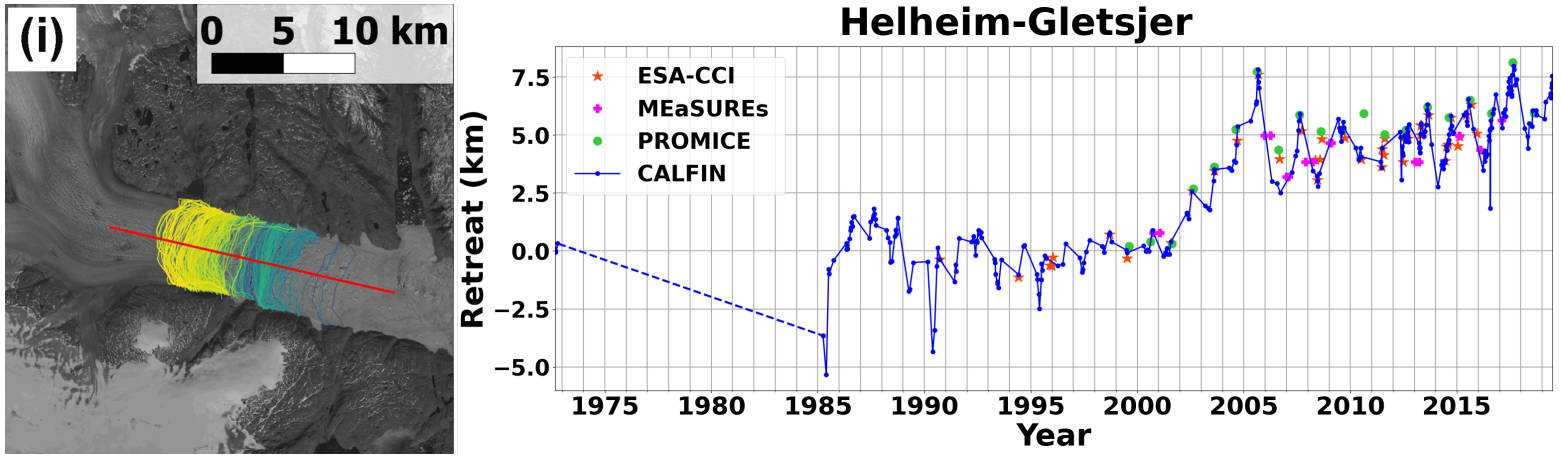

Figure A21: **Terminus Advance and Retreat Over Time for Helheim Gletsjer**. Dotted lines from 1972-1985 that indicate a lack of seasonal observations.

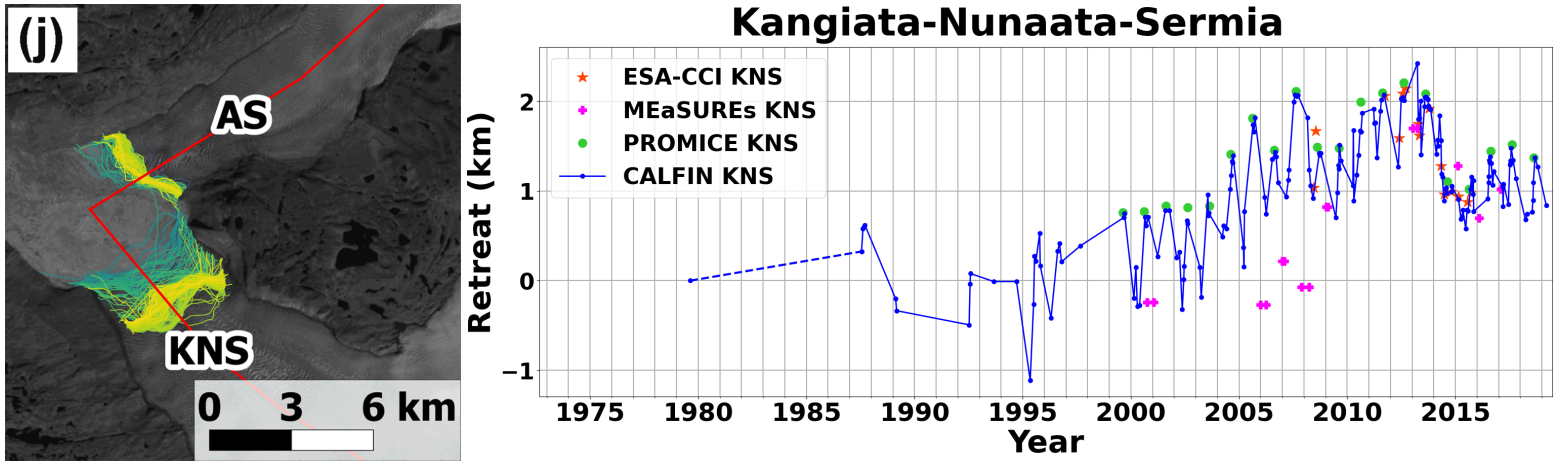

Figure A22: **Terminus Advance and Retreat Over Time for Kangiata Nunaata Sermia**. Dotted lines from 1972-1985 that indicate a lack of seasonal observations.

A.9 Regional Relative Advance and Retreat Graphs

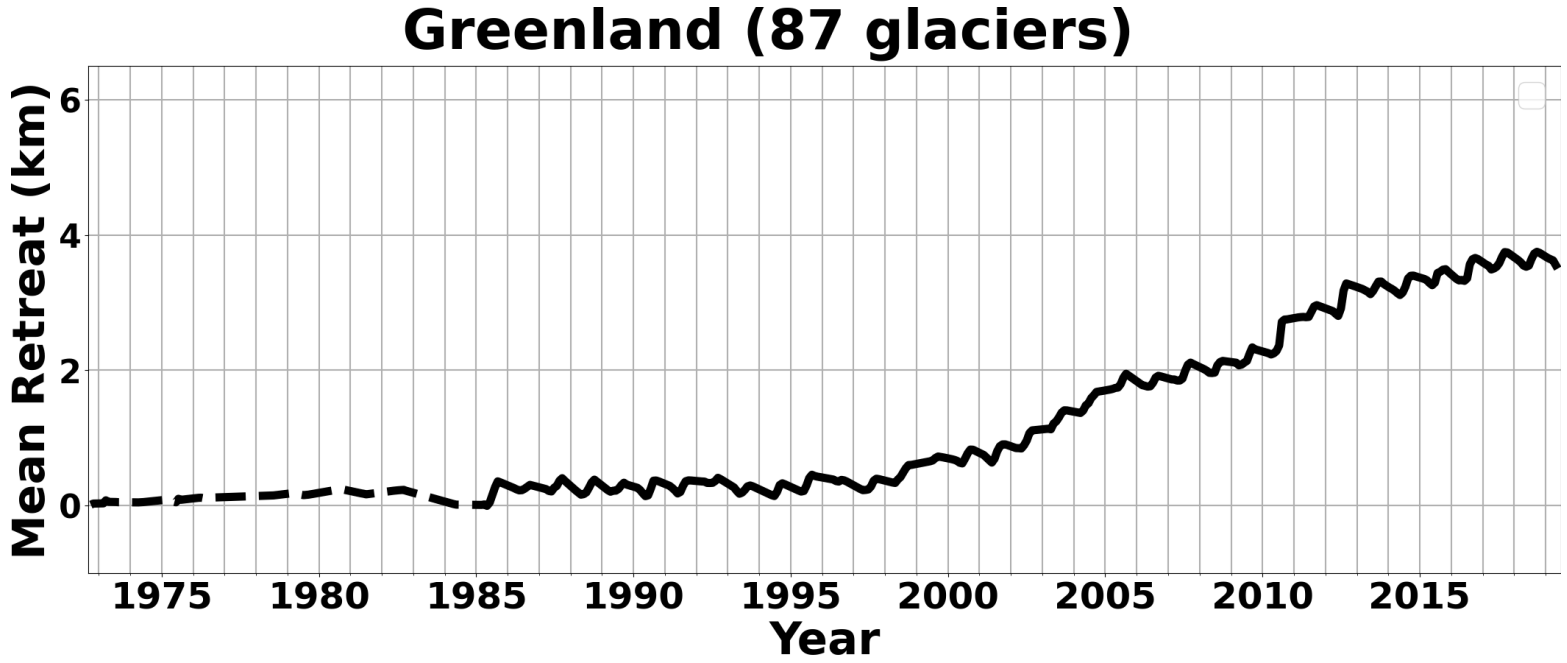

Figure A23: **Regional Terminus Advance and Retreat Over Time for Greenland**. Dotted lines from 1972-1985 that indicate a lack of seasonal observations.

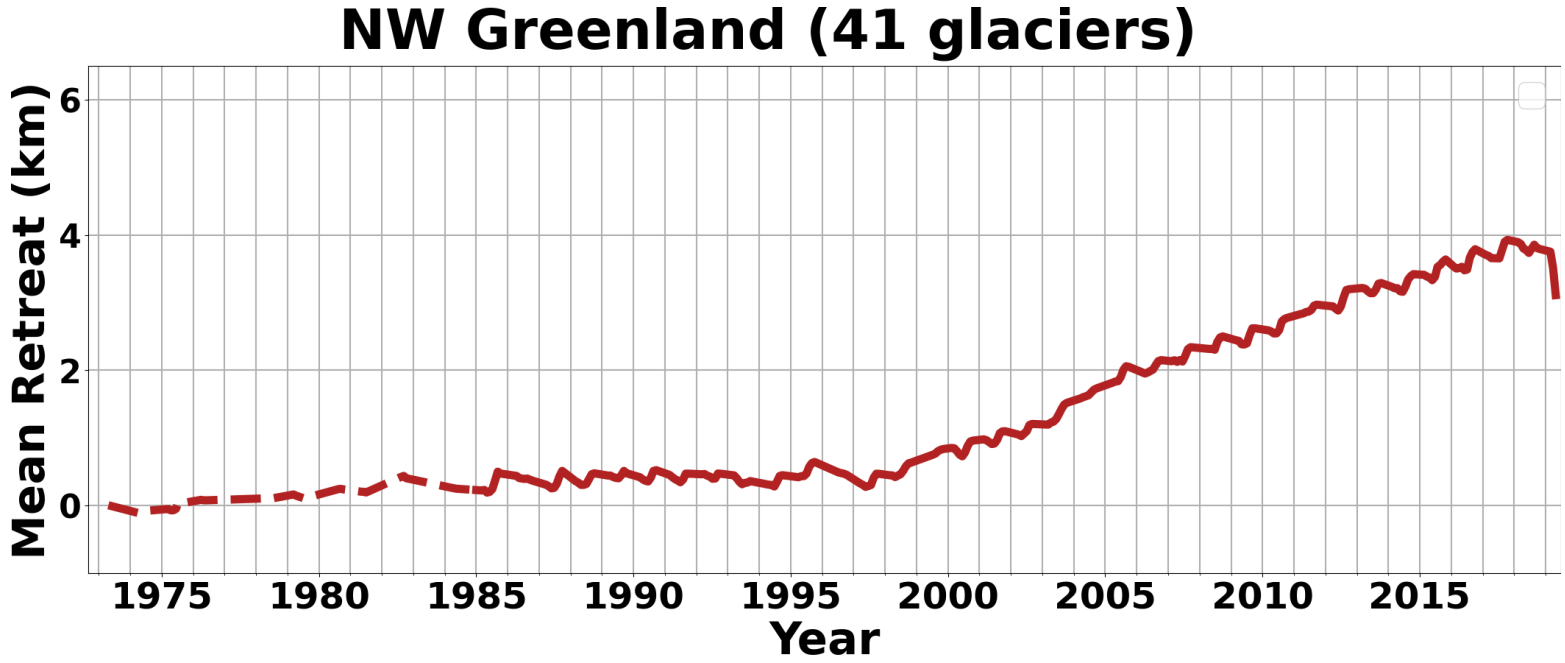

Figure A24: **Regional Terminus Advance and Retreat Over Time for NW Greenland**. Dotted lines from 1972-1985 that indicate a lack of seasonal observations.

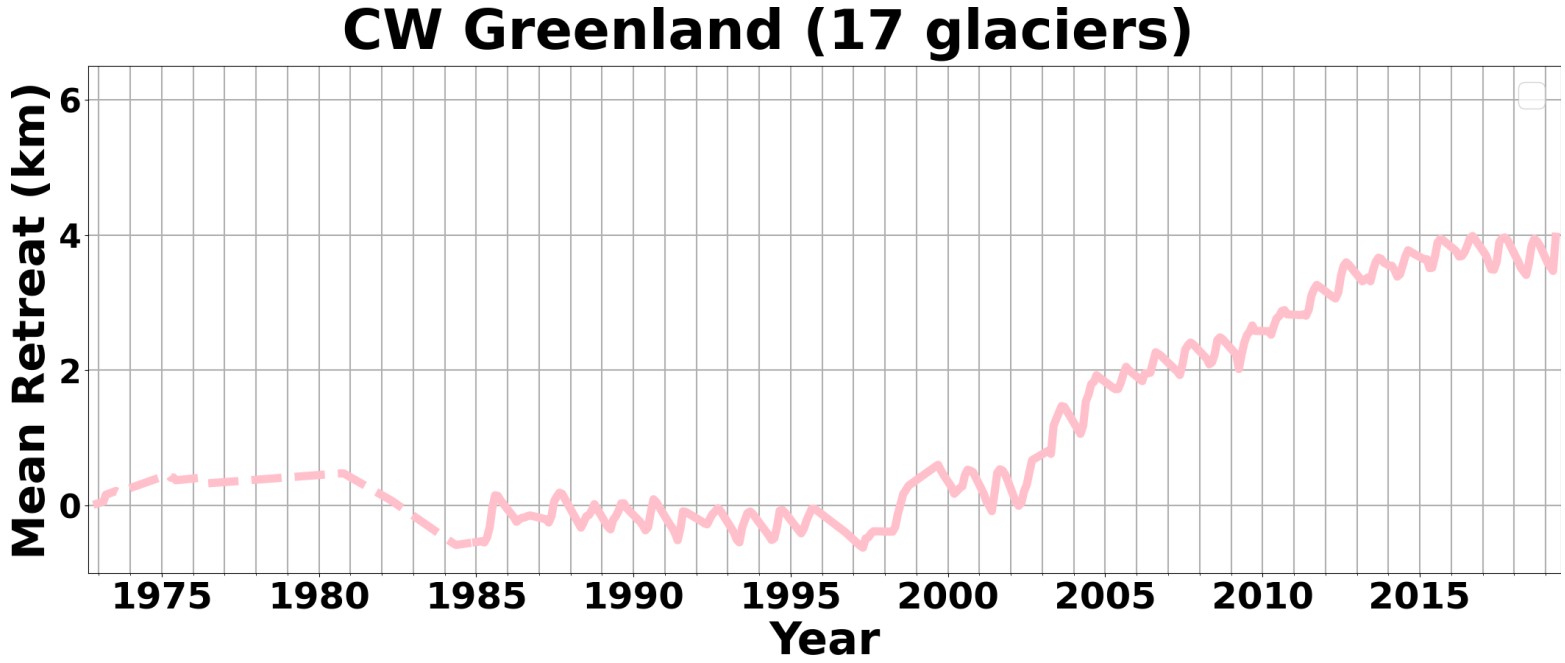

Figure A25: **Regional Terminus Advance and Retreat Over Time for CW Greenland**. Dotted lines from 1972-1985 that indicate a lack of seasonal observations.

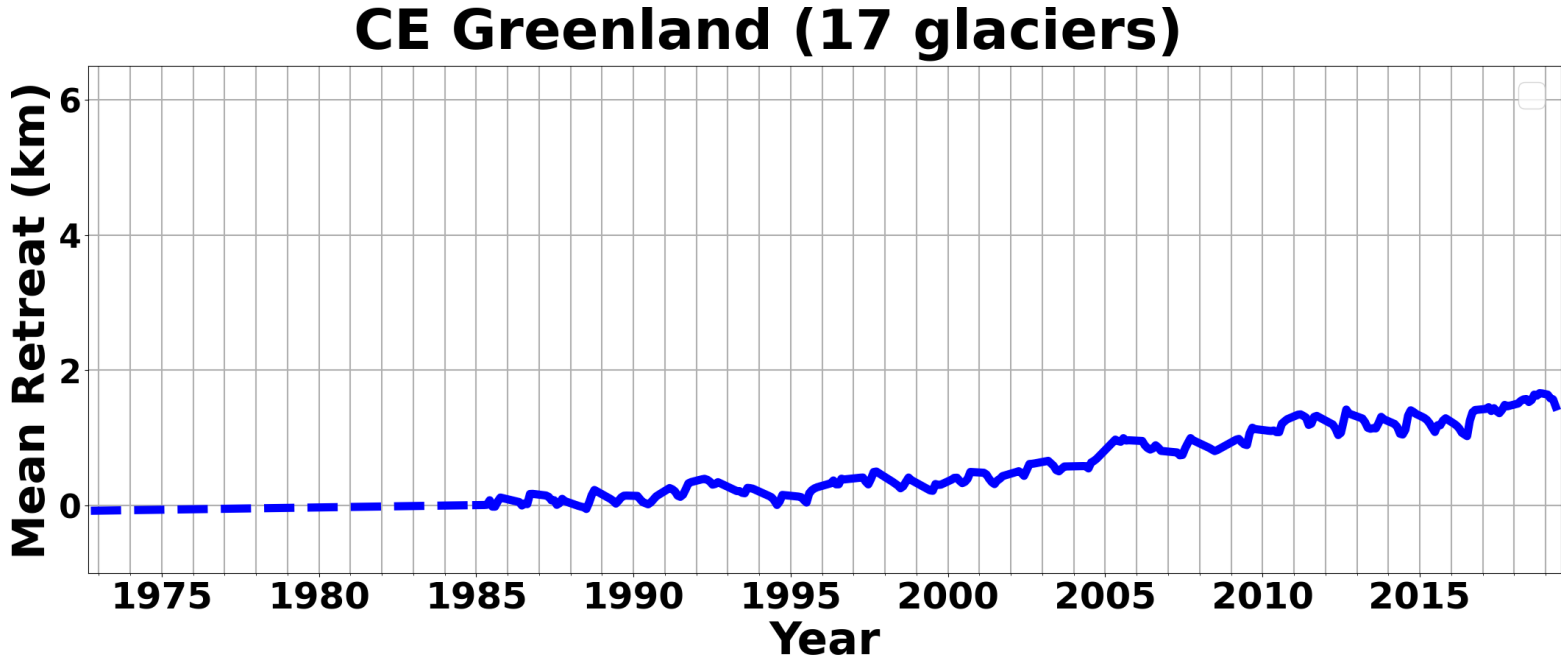

Figure A26: **Regional Terminus Advance and Retreat Over Time for CE Greenland**. Dotted lines from 1972-1985 that indicate a lack of seasonal observations.

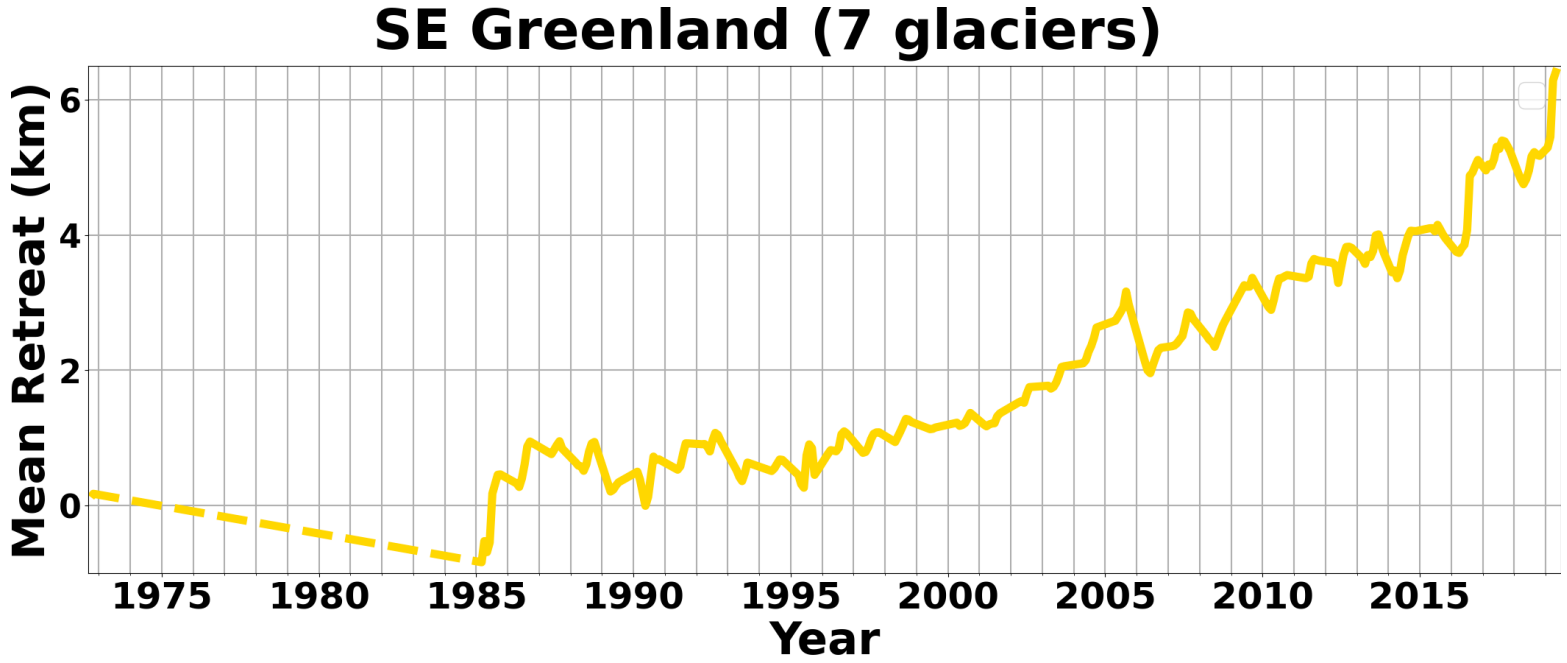

Figure A27: **Regional Terminus Advance and Retreat Over Time for SE Greenland**. Dotted lines from 1972-1985 that indicate a lack of seasonal observations.

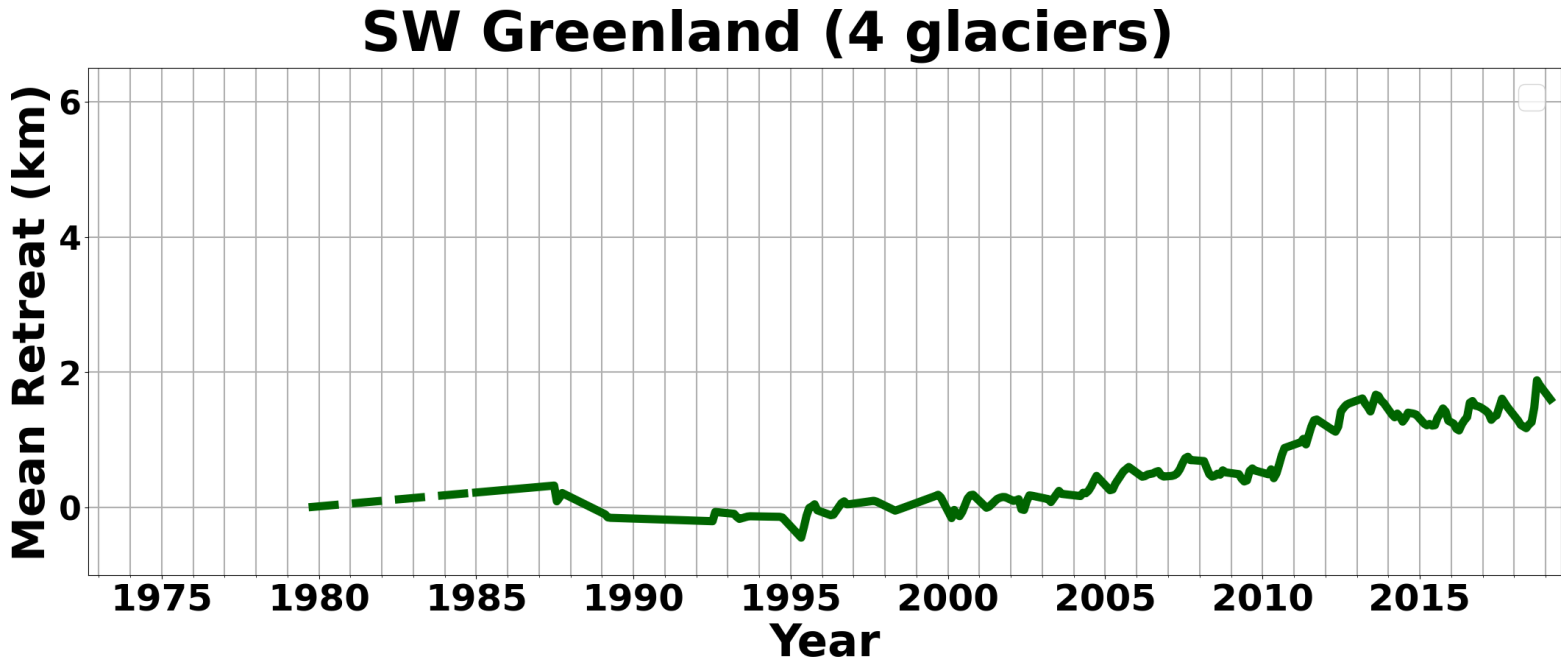

Figure A28: **Regional Terminus Advance and Retreat Over Time for SW Greenland**. Dotted lines from 1972-1985 that indicate a lack of seasonal observations.